Severe Convective Storms in Limited Instability Organized by Pattern and Distribution

TREVOR A. CAMPBELL,[a] GARY M. LACKMANN,[b] MARIA J. MOLINA,[c,d] AND MATTHEW D. PARKER[b]

[a] *Mott MacDonald, Westwood, Massachusetts*
[b] *Department of Marine, Earth, and Atmospheric Sciences, North Carolina State University, Raleigh, North Carolina*
[c] *University of Maryland, College Park, College Park, Maryland*
[d] *National Center for Atmospheric Research, Boulder, Colorado*

(Manuscript received 1 August 2023, in final form 13 December 2023, accepted 20 December 2023)

ABSTRACT: Severe convection occurring in high-shear, low-CAPE (HSLC) environments is a common cool-season threat in the southeastern United States. Previous studies of HSLC convection document the increased operational challenges that these environments present compared to their high-CAPE counterparts, corresponding to higher false-alarm ratios and lower probability of detection for severe watches and warnings. These environments can exhibit rapid destabilization in the hours prior to convection, sometimes associated with the release of potential instability. Here, we use self-organizing maps (SOMs) to objectively identify environmental patterns accompanying HSLC cool-season severe events and associate them with variations in severe weather frequency and distribution. Large-scale patterns exhibit modest variation within the HSLC subclass, featuring strong surface cyclones accompanied by vigorous upper-tropospheric troughs and northward-extending regions of instability, consistent with prior studies. In most patterns, severe weather occurs immediately ahead of a cold front. Other convective ingredients, such as lower-tropospheric vertical wind shear, near-surface equivalent potential temperature (θ_e) advection, and the release of potential instability, varied more significantly across patterns. No single variable used to train SOMs consistently demonstrated differences in the distribution of severe weather occurrence across patterns. Comparison of SOMs based on upper and lower quartiles of severe occurrence demonstrated that the release of potential instability was most consistently associated with higher-impact events in comparison to other convective ingredients. Overall, we find that previously developed HSLC composite parameters reasonably identify high-impact HSLC events.

SIGNIFICANCE STATEMENT: Even when atmospheric instability is not optimal for severe convective storms, in some situations they can still occur, presenting increased challenges to forecasters. These marginal environments may occur at night or during the cool season, when people are less attuned to severe weather threats. Here, we use a sorting algorithm to classify different weather patterns accompanying such storms, and we distinguish which specific patterns and weather system features are most strongly associated with severe storms. Our goals are to increase situational awareness for forecasters and to improve understanding of the processes leading to severe convection in marginal environments.

KEYWORDS: Convective storms; Mesoscale systems; Storm environments; Classification; Neural networks

1. Introduction

Severe convective storms in the United States take place within a broad spectrum of environmental patterns (e.g., Doswell 2001). Required ingredients for severe convection include ample moisture, instability [one measure of which is convective available potential energy (CAPE)], strong vertical wind shear, and synoptic-scale or mesoscale forcing for ascent. A subset of severe convection events take place in environments which are marginally conducive to strong convection, such as those featuring limited instability (e.g., mixed-layer CAPE $\leq$ 1000 J kg^{-1}). These high-shear, low-CAPE (HSLC) environments occur frequently, especially in the southeastern United States (e.g., Schneider et al. 2006). While the probabilities of thunderstorms and tornadoes are greater in high-CAPE environments, a large percentage of total severe thunderstorm and tornado events occur in HSLC environments, owing to their greater frequency (see Schneider and Dean 2008 for details). Prior studies have identified relatively high false-alarm ratios and low probabilities of detection for severe weather watches and warnings in HSLC environments compared to high-instability environments (Schneider and Dean 2008; Dean and Schneider 2008, 2012; Anderson-Frey et al. 2016). The geographical location of HSLC severe events also amplifies their impact, as they occur with disproportionate frequency in the southeastern United States where the population density is large and societal awareness of severe threats is relatively low (Ashley 2007; Ashley et al. 2008; Dean and Schneider 2012). Their temporal distribution also exacerbates this effect: They occur with disproportionate frequency during the cool season (Guyer et al. 2006; Schneider et al. 2006; Sherburn and Parker 2014; Sherburn et al. 2016), and during the overnight hours (Kis and Straka 2010; Sherburn and Parker 2014; Sherburn et al. 2016). Together, these factors result in a higher percentage of deadly tornadoes in the southeastern United States (3.8%) compared to the United States as a whole (2.0%; Anderson-Frey et al. 2019a).

Given the operational challenges posed by HSLC severe events, increased awareness of the variability in HSLC environmental patterns and the relation of these patterns to the

Corresponding author: Gary Lackmann, gary@ncsu.edu

DOI: 10.1175/WAF-D-23-0130.1

frequency and distribution of severe convection would be beneficial. In this paper, we apply an objective sorting algorithm to identify distinct environmental patterns associated with HSLC severe convection and determine the most critical environmental variables, quantifying the frequency and distribution of severe weather reports in association with these patterns and ingredients. Our aim is to aid forecaster pattern recognition and situational awareness, and further our understanding of key environmental conditions associated with severe weather occurrence in HSLC environments.

Earlier studies have identified the critical ingredients within HSLC environments that are conducive to severe convection (e.g., Sherburn and Parker 2014). In the southeastern United States, HSLC environments are characterized by moist boundary layers within the warm sector or ahead of cold fronts associated with strong midlatitude cyclones. The presence of strong synoptic-scale forcing for ascent accompanying a region of reduced lower-tropospheric stability (Sherburn et al. 2016; King et al. 2017) suggests the possibility of significant pattern variability within this region. In contrast, western U.S. HSLC events feature dry boundary layers near a surface triple-point or an upslope regime (Sherburn and Parker 2014; Sherburn et al. 2016).

Case studies of observed tornado-producing storms in HSLC environments reveal that midlevel dry intrusions can coincide with onset of severe convection, suggesting the release of potential instability (Lane and Moore 2006; Clark 2009; Evans 2010). Numerical simulations clarify the importance of potential instability as a factor in the rapid environmental destabilization in the hours prior to HSLC severe convection in some events, along with lower-tropospheric advection of warm, moist air, and strong 0–1-km wind shear (King et al. 2017). Destabilization can occur in time intervals ≤ 3 h prior to the arrival of convection (King et al. 2017; LaFleur et al. 2023). Two additional operational challenges associated with predicting HSLC convection are difficulty in detecting updraft rotation using radar-derived azimuthal shear at distances > 60 km from radar sites, and high false-alarm ratios associated with azimuthal shear and radar reflectivity signatures even when the storms are close to the radar (Davis and Parker 2014). The low-level mesovortices associated with QLCS events, a common convective mode in southeastern U.S. HSLC events, are shallower (Lovell and Parker 2022), often disconnected from any midlevel updraft, and are more transient (Weisman and Trapp 2003), contributing to the high false-alarm ratios. Difficulty in detecting severe weather radar signatures along with rapid destabilization in HSLC environments complicates nowcasting and warning for HSLC severe convection, notwithstanding knowledge of the generally conducive environments and ingredients.

Understanding the convective dynamics of HSLC environments is also critical to properly assess and forecast HSLC severe events. Simulations presented by McCaul and Weisman (2001) found that robust convection can occur in low-CAPE environments when there is a concentration of instability at low altitudes. Despite weaker lower-tropospheric instability, large ambient vertical wind shear supports strong low-altitude updrafts due to dynamically induced vertical perturbation pressure gradient accelerations (Sherburn and Parker 2019; Wade and Parker 2021). These strong lower-tropospheric updrafts are critical for vortex development in environments with strong vertical wind shear and marginal instability.

Over 23% of all southeastern U.S. HSLC tornadoes occur in association with quasi-linear convective system (QLCS) modes (Anderson-Frey et al. 2019a). QLCSs are narrow lines or arcs of convective storms with contiguous precipitation, often forming along cold fronts and in environments containing strong vertical wind shear (Markowski and Richardson 2010). Differences in convective mode and dynamics are evident between southeastern HSLC convection and central U.S. high-CAPE convection, with the former characterized by strong synoptic-scale forcing and lower-tropospheric destabilization that creates rapidly evolving convective features (sometimes embedded within QLCSs), whereas high-CAPE convection can be associated with weaker synoptic forcing and ample instability that is more commonly associated with cellular convective features (e.g., Smith et al. 2012).

To bridge the gap between HSLC climatologies, the dynamical processes associated with HSLC convection, and operational forecasts, several studies have examined the skill of environmental variables in discriminating between HSLC severe and HSLC nonsevere environments. Sherburn and Parker (2014) identified the 0–3-km and 500–700-hPa lapse rates as the most skillful discriminants. Combining these variables with fixed-layer shear (0–3 km) and effective-layer shear variables (SHERB and SHERBE; Sherburn and Parker 2014) while also including variables representing the release of potential instability (MOSH and MOSHE; Sherburn et al. 2016) provides forecasters with promising new tools for HSLC severe convection forecasting.

Despite the progress of many previous studies in identifying both environmental ingredients and explicit NWP proxies that are useful in HSLC convective prediction, relatively little work has been done to objectively classify variability of synoptic-scale and mesoscale patterns that accompany HSLC severe convection. Here, we address the question: Are there distinct HSLC patterns that are associated with significant variation in the frequency and distribution of severe convection? To the authors' knowledge, the only relevant objective classification involving HSLC environments was performed by Anderson-Frey et al. (2019b), who used self-organizing maps (SOMs) to classify tornadic near-storm environments in tornado outbreaks using a dataset that included southeastern U.S. HSLC events. The variance of patterns across SOM nodes was used to determine typical and atypical patterns in the significant tornado parameter (STP) for each region. They found that southeastern U.S. tornado outbreaks were often spatially displaced from maxima in STP, which may be unsurprising because the STP is in turn strongly reliant on CAPE.

The purposes of this study are to objectively classify synoptic-scale and mesoscale patterns that accompany southeastern U.S. HSLC severe convection using SOMs, and to seek variations in the frequency and distribution of severe weather across these objectively identified patterns. An additional goal is to evaluate the efficacy of HSLC composite environmental parameters such as the SHERBS3 and MOSH for severe convection across various HSLC patterns. Specifically, the analyses presented in this study are designed to address the following questions:

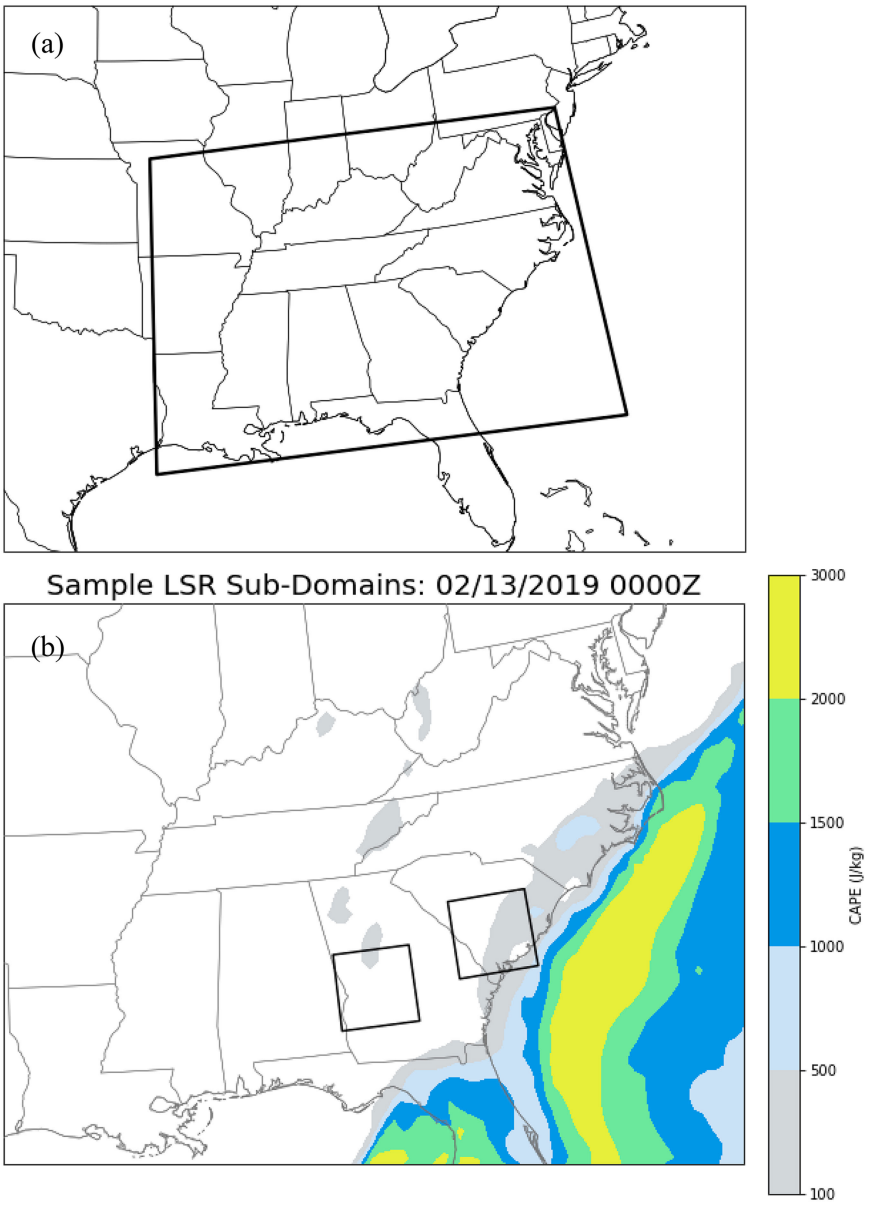

FIG. 1. (a) Study domain for HSLC severe events, bounded by 40°N, 29°N, 75°W, and 94°W. (b) Examples of Local Storm Report (LSR) subdomains used to assess local environments for HSLC criteria, for 0000 UTC 13 Feb 2019. Boxes are 200 km × 200 km centered on LSRs. CAPE is shaded as in the color bar.

(i) Are there significant variations in synoptic or mesoscale patterns that accompany southeastern U.S. HSLC severe convection?
(ii) Are there significant variations in the frequency and spatial distribution of severe weather occurrence in association with these environmental patterns?
(iii) Is the relative frequency and distribution of severe weather occurrence consistent with previously developed HSLC composite environmental parameters?

Section 2 discusses data sources, the selection criteria used in creating our HSLC severe event database, choices relating to SOMs, and definitions of analysis metrics for SOM output. Section 3 presents our results, emphasizing the variations in HSLC environmental patterns demonstrated by SOM output and the distribution of severe weather occurrence across these patterns. Key findings, operational implications, and possible future research directions are summarized in section 4.

TABLE 1. Atmospheric variables used for SOM training. Variables that were used as a part of a multivariate SOM are listed in the right column.

Training variables	Used in multivariate SOM?
500-hPa geopotential height	Yes (with sea level pressure)
Sea level pressure	Yes (with 500-hPa geopotential height)
700–1000-hPa θ_e difference	Yes (with 500-hPa vertical velocity)
MUCAPE	No
0–6-km vertical wind shear	No
0–1-km vertical wind shear	No
0–1-km storm relative helicity	No
Near-surface temperature advection	No
Near-surface dewpoint temperature advection	No
Near-surface θ_e advection	No
500-hPa vertical velocity	Yes (with 700–1000-hPa θ_e difference)
SHERB	No
MOSH	No

2. Data and methods

a. Event selection

We used an automated algorithm to generate a 13-season catalog of HSLC severe events in the southeastern United States, defining HSLC events as 6-h windows that met specific criteria. The windows are 6-h periods beginning 0000, 0600, 1200, or 1800 UTC. Consecutive 6-h windows were considered to be independent meteorological events based on the rationale that the environmental patterns at different stages of storm development could vary in meaningful ways. Given that HSLC environments occur primarily in the southeastern United States (Schneider et al. 2006), a domain bounded by 40°N, 29°N, 75°W, and 94°W was selected as our analysis region (Fig. 1a). We define the cool season as 1 October–30 April; our dataset spans the cool seasons from 2008/09 through 2020/21. The process of identifying HSLC severe events was automated using a two-step Python script that checks the National Centers for Environmental Information's (NCEI) Storm Events Database (NCEI 2008) for Local Storm Reports (LSRs) and National Centers for Environmental Prediction (NCEP) 20-km Rapid Refresh/Rapid Update Cycle (RAP/RUC) analysis data (NOAA/NCEP 2005) obtained from NCEI.

We designed the algorithm to first identify the presence of severe wind and tornado reports within the study region. All 6-h windows were searched for LSRs within the domain. Previous studies document the limitations of LSRs, including biases due to heterogeneous population density, and inconsistent reporting practices (Brooks et al. 2003; Doswell et al. 2005; Trapp et al. 2006). An additional limitation is the unavoidable lack of reporting over water. A possible alternate data source for identifying severe convection is radar-derived rotation tracks, which have some advantages over LSRs (e.g., Dawson et al. 2017). However, for HSLC convection there are serious limitations in detection at distances greater than 60 km from a radar site owing to the small horizontal and vertical dimension of many HSLC convective storms (Davis and Parker 2014). Hail reports were excluded from our analysis because significant hail (>3/4 in.) is not expected to be the primary hazard in these environments, being more commonly associated with high-instability environments (Schneider and Dean 2008). Wind reports were included because convective modes prevalent in HSLC environments (e.g., QLCS) often produce damaging winds, although we note that there are biases related to overestimation of wind gusts in the southeastern United States (Edwards et al. 2018). Given the above, if one or more tornado or wind report occurred within a 6-h window in the study region, that 6-h window was identified as a "severe event." Our intent in setting this low threshold is to include low-impact events, allowing greater event diversity and stratification by varying levels of LSR activity.

Next, our algorithm used RUC/RAP analyses to determine if a given severe event met HSLC criteria, using the environments in the vicinity of individual LSRs (e.g., Fig. 1b). We used thresholds of most unstable CAPE (MUCAPE) ≤ 1000 J kg^{-1} and 0–6-km wind shear ≥ 18 m s^{-1} to delineate HSLC environments, as in previous studies (Sherburn and Parker 2014; Sherburn et al. 2016; King et al. 2017; Graham 2021). By excluding hail reports and eliminating high MUCAPE cases, we are effectively eliminating cases characterized by elevated convection. We selected MUCAPE for our analysis because it is the most stringent cutoff for what constitutes low-CAPE events. Early in the analysis period we used 20-km RUC analyses; the RAP was commissioned in May 2012, so subsequent events use RAP analyses. An advantage of the RUC/RAP analyses are reasonably high spatial resolution (20-km grid length) and hourly temporal frequency. The analysis data

TABLE 2. Hyperparameters used in the SOM training process.

Hyperparameter name	Hyperparameter setting
Input length	453
Learning rate	0.5
Decay function	Asymptotic decay
Neighborhood function	Gaussian
Topology	Rectangular
Activation distance	Euclidean
Random seed	1
No. of iterations	100 000
Random order	True

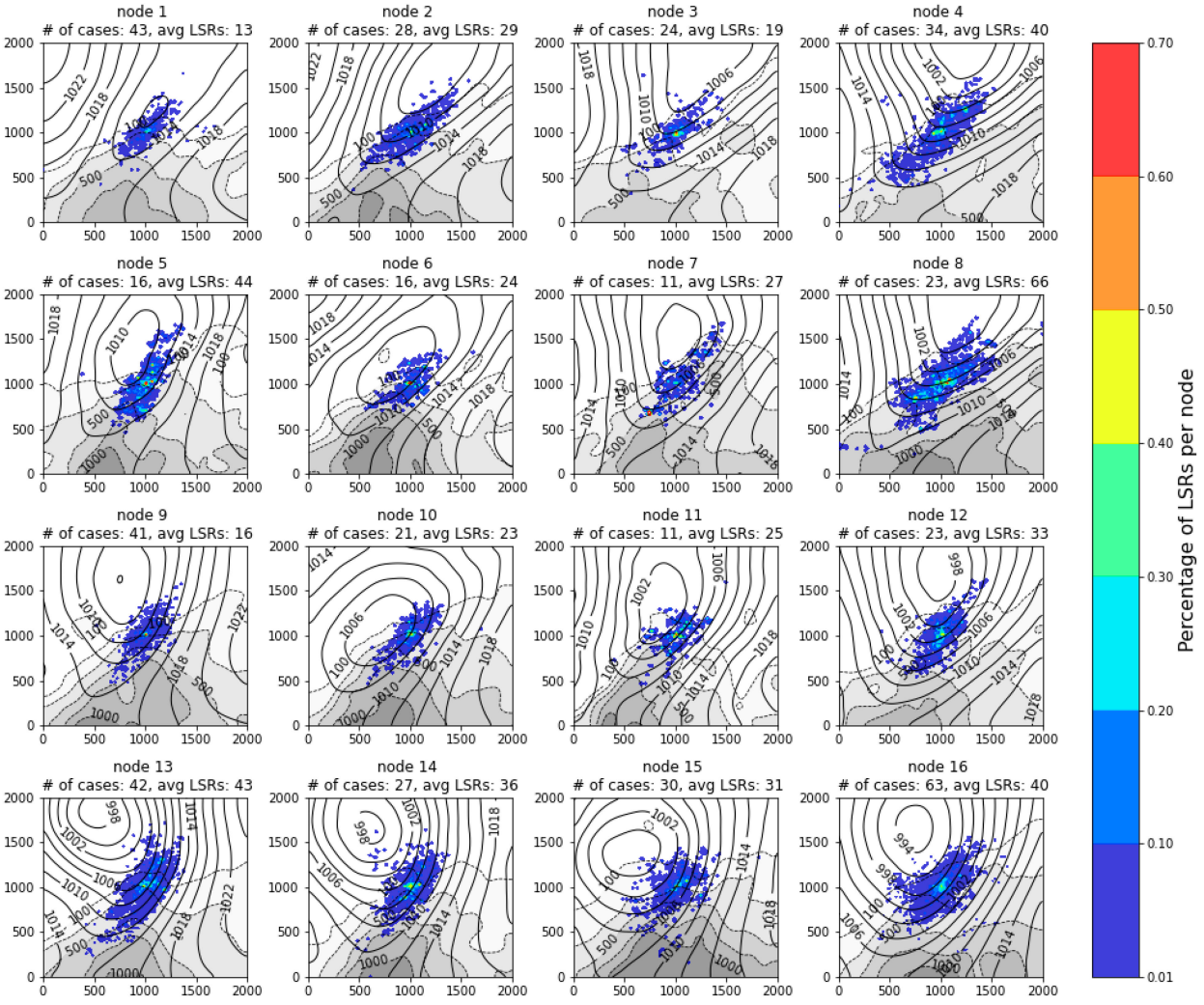

FIG. 2. SOM trained on sea level pressure (SLP; hPa) for HSLC severe events. Data are event-relative 2000 km × 2000 km grids centered on the event-averaged storm report latitude and longitude. Pressure is contoured in solid black every 2 hPa, node composite MUCAPE is shaded and dash contoured every 500 J kg^{-1}, and LSRs are plotted as the percentage of cases where wind and tornado LSRs occur at in a given grid cell, shaded as in the color bar. Total number of events and the average number of wind and tornado LSRs for each node is listed above each node; axis labels are in kilometers.

were taken from the event onset time (0000, 0600, 1200, or 1800 UTC) to measure the environment surrounding the severe reports prior to a period of severe convection, as would be seen by a forecaster. All LSRs within each event were adjusted from a latitude and longitude coordinate to the closest RUC/RAP analysis data grid cell via a nearest neighbor approach. Then, a 200 km × 200 km subgrid around each adjusted LSR was created to represent the respective LSR's local environment (Fig. 1b).

We designed our algorithm to then categorize the severe events identified as described above into three categories: (i) severe events in which all LSRs occur within an HSLC environment, (ii) severe events with no LSRs occurring in an HSLC environment, and (iii) severe events with LSRs in both HSLC and non-HSLC environments. We retain all of the first category events and apply conditions to select some of the third category events for our HSLC case catalog. The first two categories are defined using spatially averaged MUCAPE $\leq$ 1000 J kg^{-1} and 0–6-km wind shear $\geq$ 18 m s^{-1}. For the third category, to accommodate events where strong gradients of CAPE or wind shear were present within the LSR's local environment ("subgrid") or where significant geographic spread in LSRs resulted in notably different local environments, all LSR CAPE and wind shear subgrids for a given severe event were averaged. If HSLC criteria were met on this averaged grid, the severe event was included in the HSLC case catalog. For category iii events that did not meet this additional criterion, if the ratio of HSLC LSR subgrids to non-HSLC subgrids was $\geq$5, the event was also included. All other category iii events were eliminated. Out of 11 027 possible 6-h windows over 13 cool seasons, we identified 453 HSLC severe events having at least one

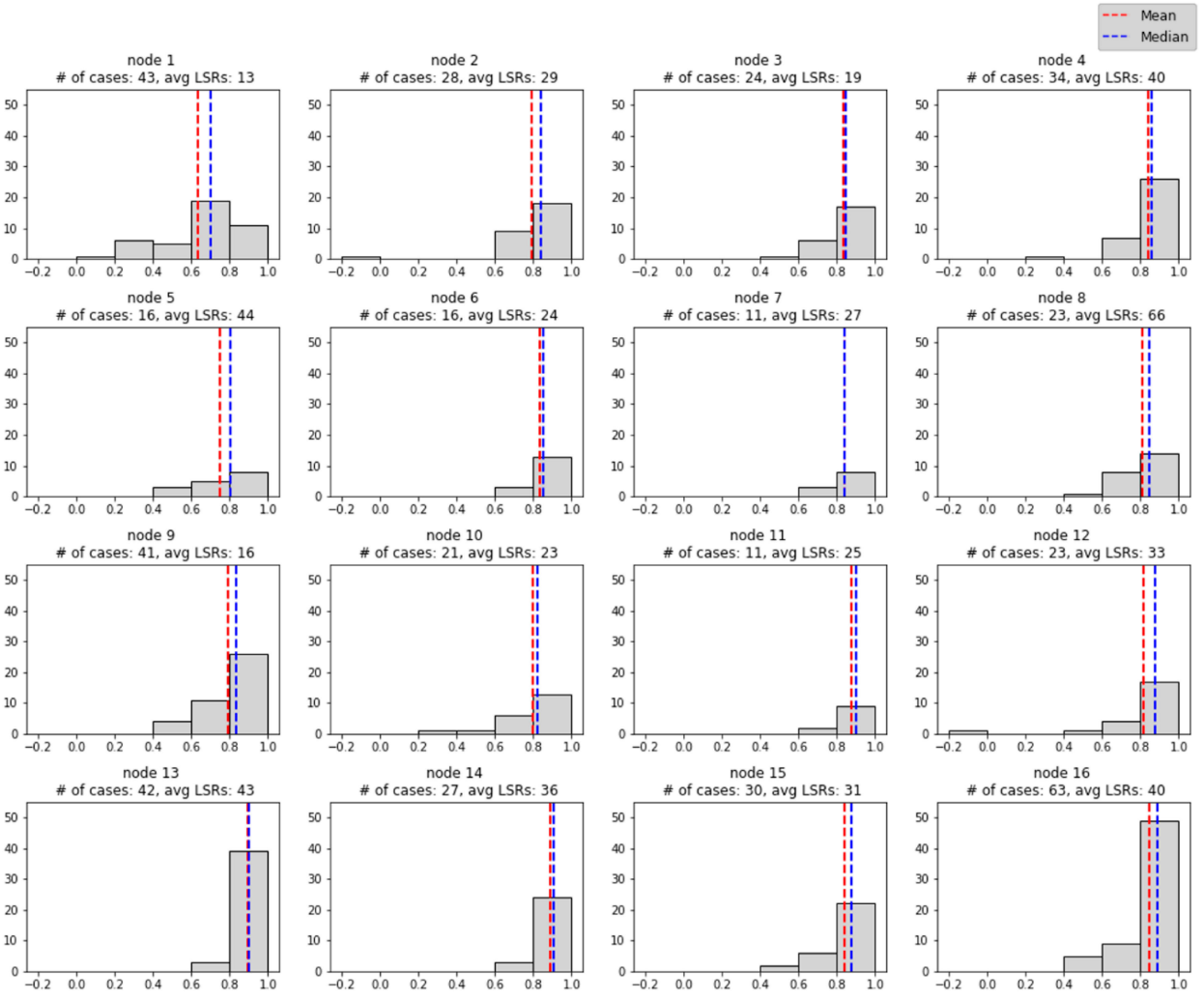

FIG. 3. Histogram plots depicting the correlation coefficients for all cases within the respective best-matched node with respect to the node composite for the SLP trained SOM. The mean correlation coefficient in a node is indicated with a red dashed line and the median correlation coefficient in a node is indicated with a blue dashed line, as in the legend (top right).

tornado or severe wind report in the southeastern U.S. domain. This large HSLC dataset was cross-checked against earlier HSLC event lists compiled by Sherburn and Parker (2014) and Graham (2021) and was found to provide an adequate match (Campbell 2022).

b. *Self-organizing maps*

SOMs are an unsupervised machine learning technique that trains a neural network using competitive learning and maps an input dataset to a user-specified number of nodes (Kohonen 2001). Nodes are vectors made up of "weights," where weights are values that are updated toward the input data during the training process. The number of weights in a node is the same as the number of values in one sample of the input dataset. SOMs have been used in a wide variety of meteorological studies for classification of synoptic-scale and climate patterns (e.g., Hewitson and Crane 2002; Schuenemann et al. 2009; Mechem et al. 2018; Loikith et al. 2022; Radford and Lackmann 2023), as well as for study of severe convection (e.g., Nowotarski and Jensen 2013; Nowotarski and Jones 2018; Anderson-Frey et al. 2019b; Goldacker and Parker 2021). The SOM training process begins with selection of a user-defined number of nodes, followed by random initialization of the node weights (e.g., Vesanto and Alhoniemi 2000). Prior to training, all data are normalized using a z score:

$$z = \frac{z_{i,j} - \overline{z}}{\sigma_z}, \tag{1}$$

where $z_{i,j}$ is the two-dimensional field of a variable for a given event, $\overline{z}$ is the mean of the variable across all events, and σ_z is the standard deviation of the variable field across all events.

Once defined, the SOM training starts by selecting a sample from the input dataset and computing the similarity between the values of the respective sample and each of the node

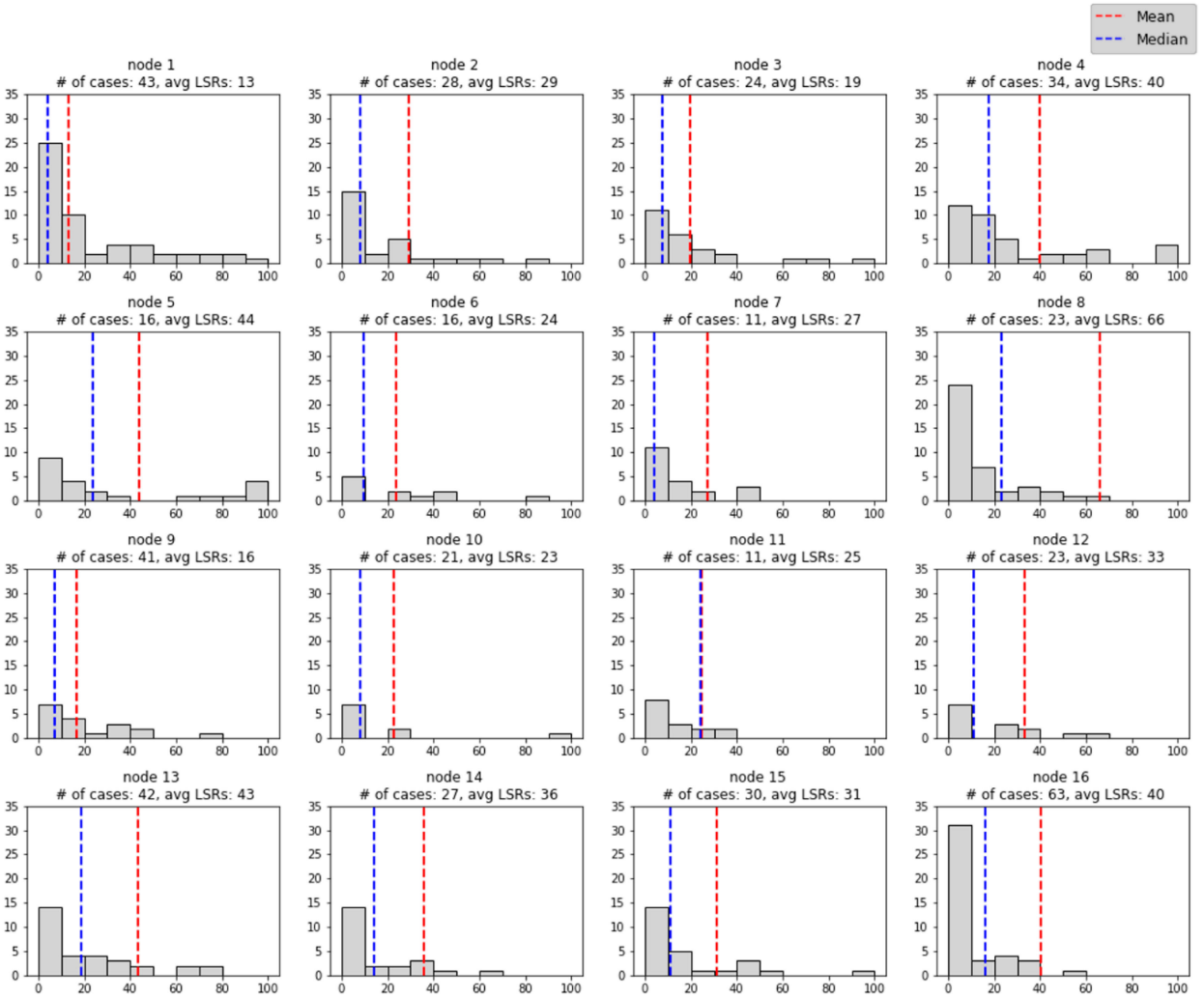

FIG. 4. Histogram plots depicting the frequency of LSRs for cases within the respective best-matched SLP trained SOM node. Histograms are clipped at 100 LSRs to improve clarity. The mean number of LSRs in a node is indicated with the red dashed line and the median number of LSRs in a node is indicated with a blue dashed line, as in the legend (top right).

weights, where similarity is measured using Euclidean distance. A node is assigned as the "winning node" when Euclidean distance is smallest between the node weights and the sample's values. The weights of the winning node and its neighbors are then updated using a predefined learning rate, with weights adjusted toward the sample's values. The radius of neighboring nodes that are updated is a user-defined value named sigma (σ). This process of updating node weights is repeated for all input data samples over a user-defined number of iterations. As this process is repeated, the node weights become more like the input dataset with similar cases grouped in the same node. Importantly, the learning rate and σ are asymptotically decreased as the number of training iterations increases, which characterizes the competitive learning aspect of training; nodes that neighbor winning SOM nodes no longer update (or do very little) during final training iterations.

Here, we use version 2.2.9 of the MiniSom Python module (Vettigli 2018) to create SOMs trained on a set of atmospheric variables (Table 1) to define the patterns that accompany southeastern U.S. HSLC severe convection. These atmospheric variables were selected in keeping with previous studies, which identify strong synoptic forcing as a key ingredient in producing severe convection (Sherburn et al. 2016), along with surface warming and moistening, lower-tropospheric forcing for ascent, and the release of potential instability (King et al. 2017). In addition to typical meteorological diagnostics, we also train SOMs using two multivariate environmental predictors for HSLC severe convection: severe hazards in environments with reduced buoyancy with 0–3-km shear magnitude (SHERBS3) (Sherburn and Parker 2014) and modified SHERB (MOSH) (Sherburn et al. 2016). The SHERBS3 [(2)] is a composite parameter designed to separate significant HSLC severe convection from nonsevere HSLC storms using a threshold of 1.0 (significant severe weather is more likely for SHERBS3 > 1):

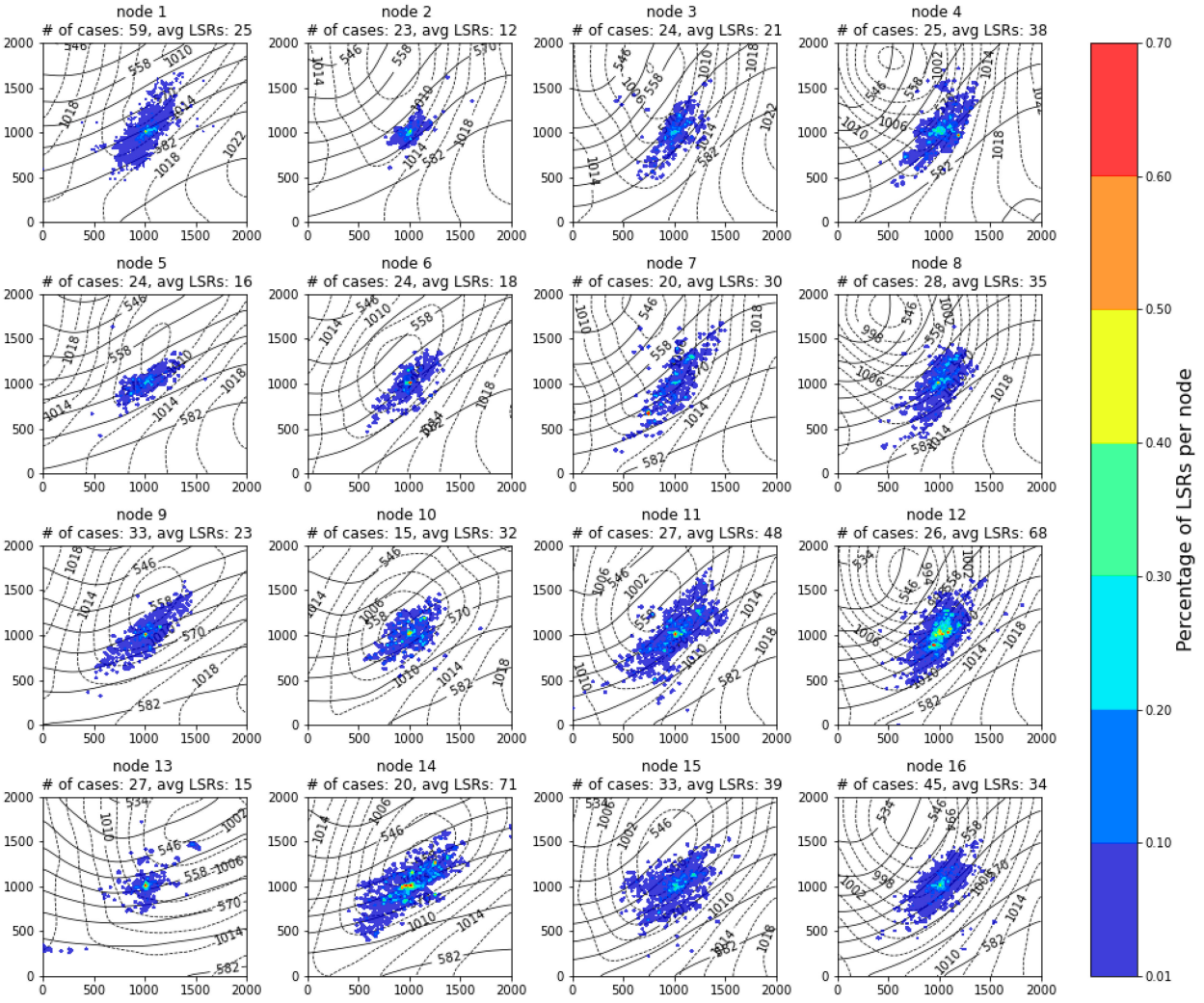

FIG. 5. Event-relative, multivariate SOM trained on 500-hPa geopotential height and SLP. Geopotential height is contoured in solid black every 6 dam and SLP is contoured in dashed black every 2 hPa. LSRs are plotted as in Fig. 2; axis labels are in kilometers.

$$\text{SHERBS3} = \frac{\text{S3MG}}{26\ \text{m s}^{-1}} \times \frac{\text{LLLR}}{5.2\ \text{km}^{-1}} \times \frac{\text{LR75}}{5.6\ \text{km}^{-1}}. \quad (2)$$

Here, S3MG is the 0–3-km shear magnitude, LLLR is the 0–3-km lapse rate, and LR75 is the 700–500-hPa lapse rate (Sherburn and Parker 2014).

The MOSH is a composite parameter designed to improve upon the SHERB by including a proxy for destabilization resulting from the release of potential instability:

$$\text{MOSH} = \frac{(\text{LLLR} - 4\ \text{K km}^{-1})^2}{4\ \text{K}^2\ \text{km}^{-2}} \times \frac{(\text{S15MG} - 8\ \text{m s}^{-1})}{10\ \text{m s}^{-1}} \times \frac{(\text{MAXTEVV} + 10\ \text{K Pa km}^{-1}\ \text{s}^{-1})}{9\ \text{K Pa km}^{-1}\ \text{s}^{-1}}. \quad (3)$$

In (3), S15MG is the 0–1.5-km shear magnitude, and MAXTEVV is the maximum $(d\theta_e/dz) \times \omega$ product calculated from the 0–6-km layer at 0.5-km intervals (Sherburn et al. 2016). Sherburn and Parker (2014) and Sherburn et al. (2016) also provide composite variables calculated using effective bulk shear (Thompson et al. 2007, 2012). Here we prioritize the fixed layer MOSH and SHERBS3 as it used by forecasters due to the current inability to calculate effective bulk shear products in real time (K. Sherburn 2022, personal communication).

We used two methods of formatting the SOM input data for different environmental classification processes, both using the previously mentioned RAP/RUC analysis data at the event onset time. The first method was creating an event-relative 2000 km × 2000 km data subset centered on the average LSR latitude and longitude coordinate for each event and converting that coordinate to the closest RAP/RUC analysis grid point. This was designed to capture LSR frequency and distribution in relation to meteorological features. Despite the relatively large size of the subset and its location in the southeastern United States, there were no instances in which the event-relative data subset intersected the edge of RAP/RUC data domain. The second method

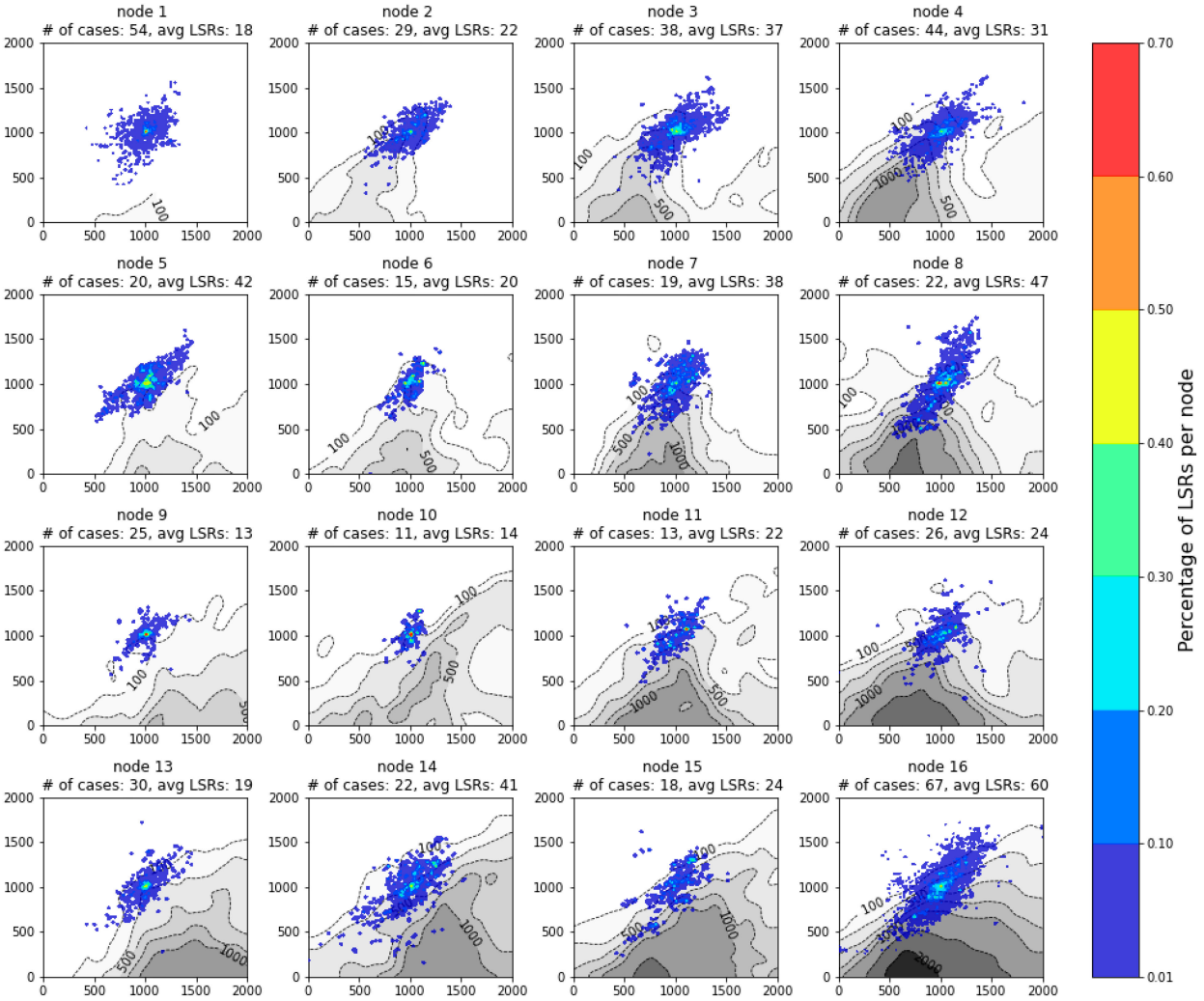

FIG. 6. SOM trained with MUCAPE; MUCAPE is contoured and shaded every 500 J kg^{-1}. LSRs are plotted as in Fig. 2.

was using the southeastern U.S. event identification domain as a fixed domain (Fig. 1a), designed to relate the LSR frequency and distribution to geographic features. For both methods, all SOMs were trained using the atmospheric variables outlined in Table 1. For brevity, only SOMs trained with event-relative data are presented here. The fixed domain SOMs exhibited a similar sample of environmental patterns throughout all training variables as compared to the event-relative SOMs. The primary difference was in SOM orientation, where the organization of SOM nodes sorted meteorological features based on their location within the domain, resulting in a longitudinal shift in LSRs across SOM nodes (not shown).

While SOMs provide a powerful tool for objective sorting of patterns, they also accommodate a daunting number of possible training variables and strategies. A single training variable can be used to train a SOM, with additional corresponding composites of other variables displayed for the various nodes. When a set of meteorological patterns are sorted by the SOM software, every case fits into one of the nodes (i.e., each sample is assigned to a winning node), and for unique or outlier cases, this can lead to intra-SOM node distortion and variability. This is quantified across the entire SOM via the quantization error (described in the following paragraph), but it is also helpful to consider variability within each node.

Determining the desired number of nodes for SOM analysis required making trade-offs: Too few SOM nodes could result in excessive smoothing of distinct environmental patterns within each node, and too many nodes could result in repetition of similar environmental patterns across multiple SOM nodes. To optimize the number of nodes, we used a combination of quantitative analysis of error metrics (quantization and topographic error) and qualitative assessment via sensitivity tests. Quantization error is related to the degree of fit of each pattern to its winning (i.e., best-matched) node, while topographic error defines organization of the SOM by considering the number of samples whose runner-up matched node is nonadjacent to its best-matched node. Calculating these error metrics for all SOMs trained using different input variables demonstrated

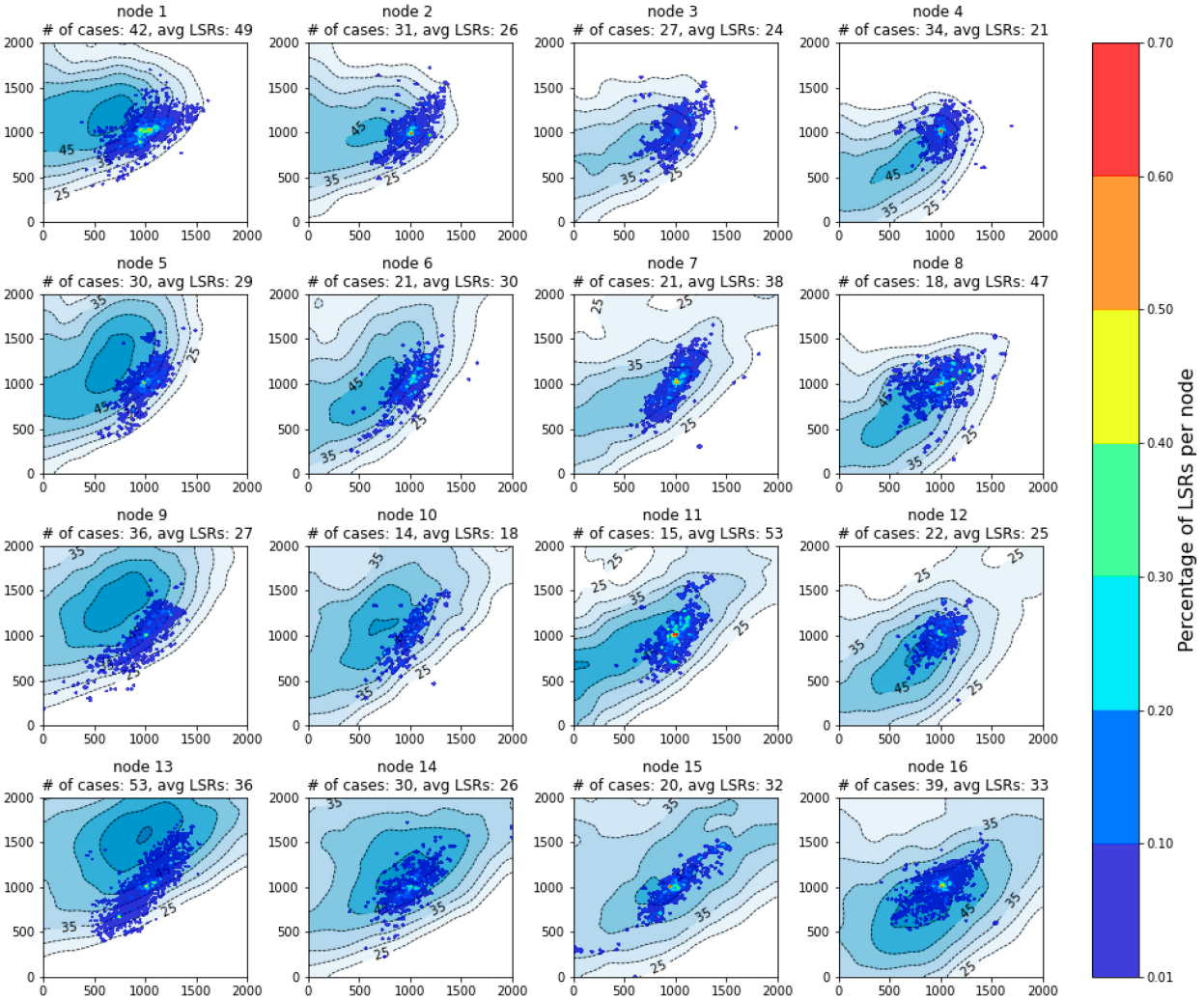

FIG. 7. SOM trained with 0–6-km vertical wind shear. Vertical wind shear is contoured and shaded every 5 kt. LSRs are plotted as in Fig. 2.

variability that is highly dependent on the "smoothness" of the training variable. For example, a 4 × 4 dimension SOM trained on a smoother variable such as 500-hPa geopotential height has a lower quantization error than the SOM trained using a noisier variable such as near-surface temperature advection. A 4 × 4 SOM dimension was most consistent in capturing distinct and physically meaningful patterns and was thus selected for use in much of our analysis. The remaining "hyperparameters" (i.e., user-defined parameters that control the learning process) used in the SOM training process were kept constant throughout all experiments presented in this study [Table 2, see also Campbell (2022, his section 2.2)]. To further describe SOM representativeness of physically meaningful patterns, we computed the correlation coefficient between each sample within a best-matched node and the respective node composite for all variables. Considering the mean and median of correlation coefficients helps us to understand which nodes are the most representative in an individual SOM, and serves to support the quantization error results, providing insight into which training variables yield more representative SOM nodes on average.

c. *Impact metrics*

Impact metrics were calculated to determine the variation in severe weather frequency between SOM nodes. Given that tornado and wind LSRs were used in this study to characterize severe weather, the impact metrics were defined by the spread of the total number of LSRs across all events (i.e., samples) within a node. We used the variability in mean and median values of total LSRs across nodes to seek meteorological patterns that are especially conducive to severe weather occurrence. We calculated these quantities for both total LSRs and tornado-only LSRs to assess whether particular patterns are more or less conducive to tornadoes.

To provide a visual representation of severe weather reports for each pattern, we used a nearest-neighbor approach

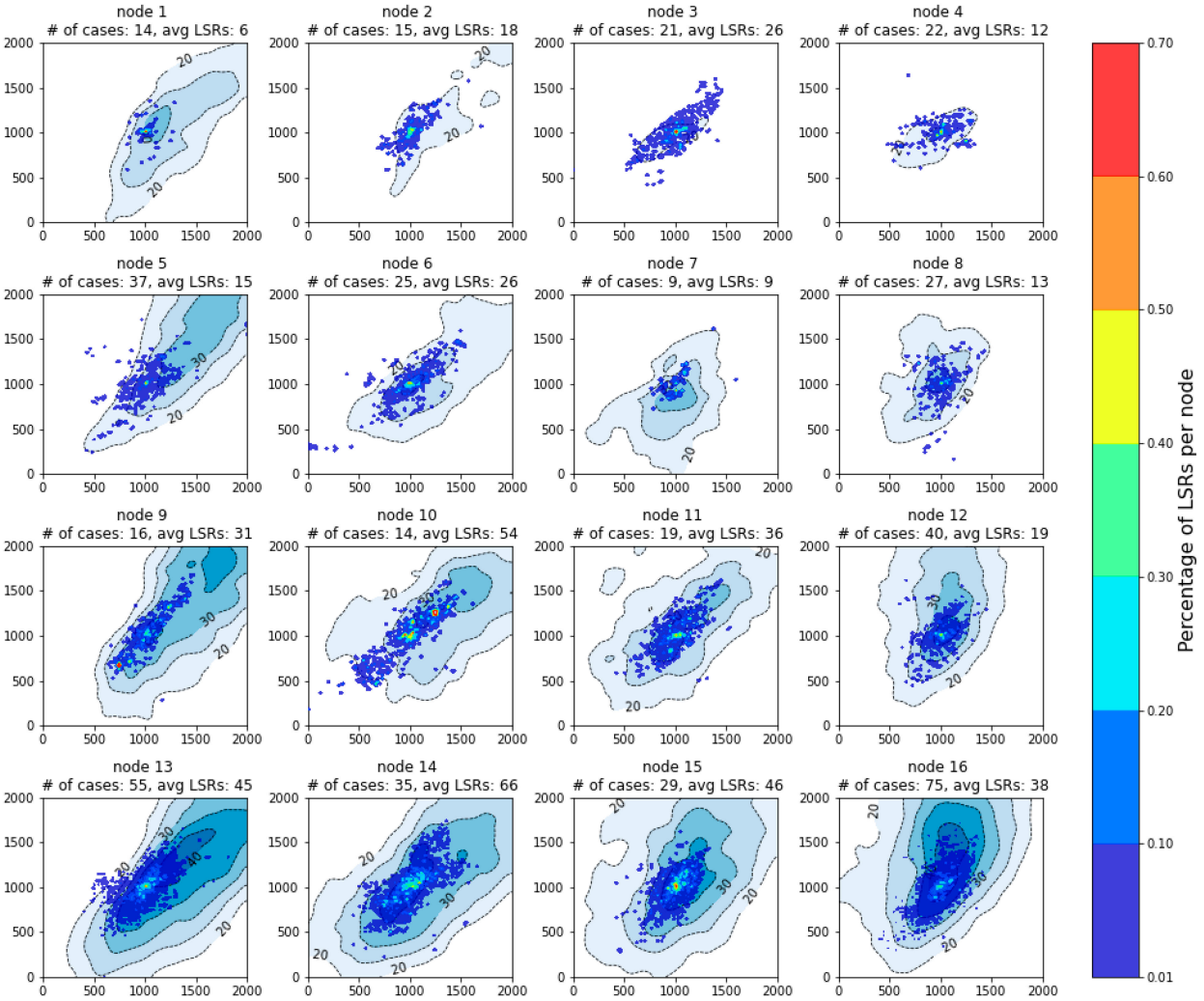

FIG. 8. SOM trained with 0–1-km vertical wind shear; vertical wind shear is contoured and shaded every 5 kt. LSRs are plotted as in Fig. 2.

to identify the grid locations of the LSRs, and computed LSR density. This is displayed at each grid cell as the ratio of LSRs in that grid cell to the total number of events in that SOM node. Given that the data are event relative, the maximum values of LSR density are generally found near the center of the domain. However, assessing the spatial distribution of LSR density compared to the orientation of given meteorological features clarified the relative locations of severe reports to these features.

To further distinguish between the environmental patterns associated with varying impact (defined by LSR count), a final set of SOMs was trained on the upper- and lower-quartile LSR events. The upper quartile was defined as events with ≥36 LSRs and the lower quartile was defined as events with ≤4 LSRs. Given the reduced number of events in the respective datasets, additional error metric sensitivity testing led us to select a SOM dimension of 3 × 3 for this part of the analysis.

3. Results

a. *Overall LSR distribution relative to HSLC meteorological fields*

To provide a basic view of the synoptic-scale patterns accompanying HSLC severe convection, we first present a SOM trained using sea level pressure and overlay composite MUCAPE and LSR density (Fig. 2). This SOM is organized by trough and cyclone location, orientation, and intensity, with southwest–northeast-oriented troughs in the upper nodes, and more intense cyclones in the lower right. The average number of LSRs per node generally increases with cyclone intensity. Each SOM node is viewed as a mean composite, subject to signal smoothing and variability. To quantify this, we computed the correlation coefficient between each event in a best-matched node and the respective node mean for the training variable (Fig. 3); this reveals that the lower and right SOM nodes in Fig. 2 exhibit strong intranode correlation (the mean and median of the

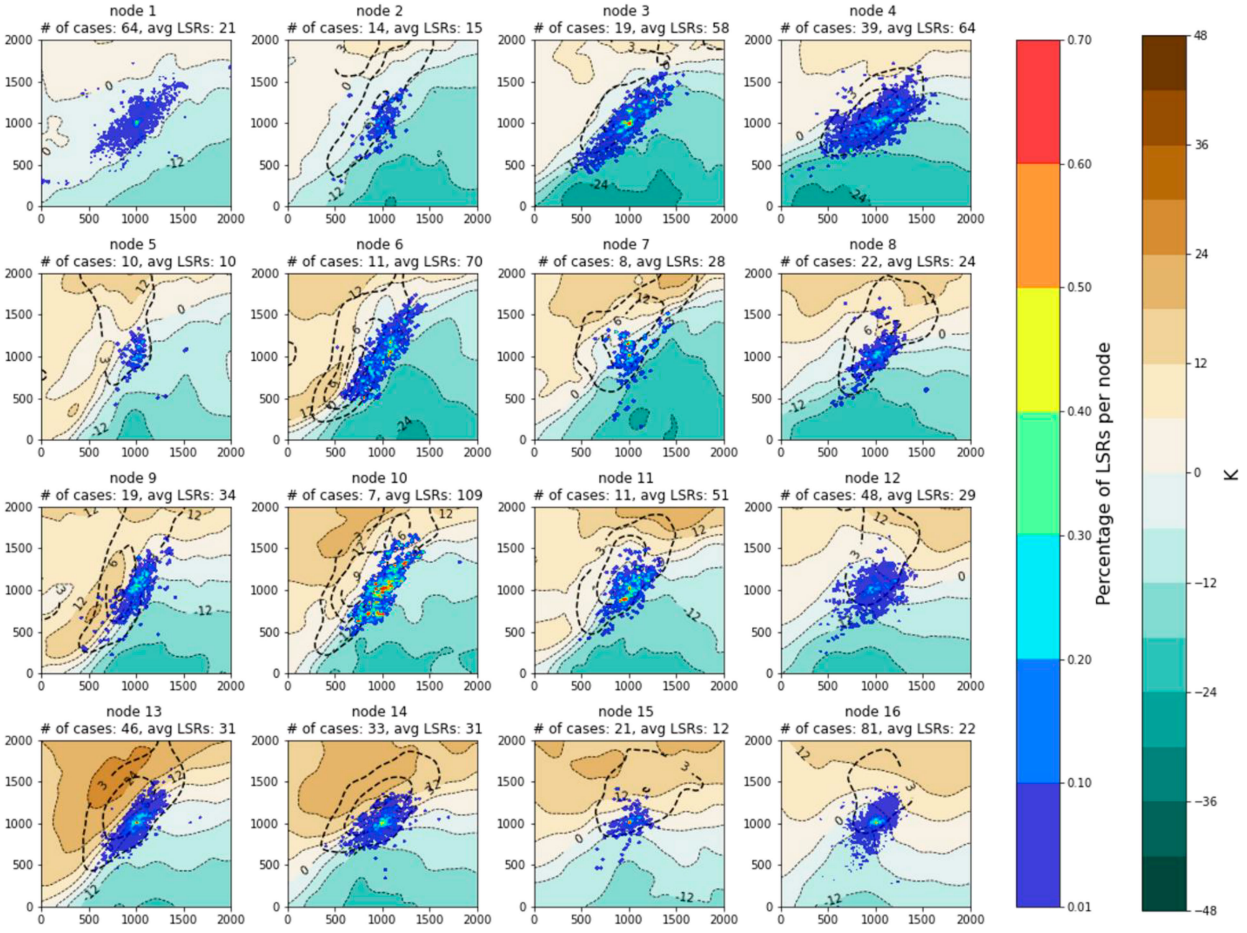

FIG. 9. Multivariate SOM trained with 700–1000-hPa θ_e difference and 500-hPa vertical velocity. The θ_e difference is shaded every 6 K as in the color bar (far right), and vertical velocity is contoured every 3 μb s^{-1}, with only ascent contours plotted. LSRs are plotted as in Fig. 2.

correlation coefficient are nearly 0.9), while the upper left nodes exhibit considerably more intranode variability (mean and median correlation coefficient < 0.7). We also consider the statistical distribution of each event's LSRs across this SOM (Fig. 4). Despite the tendency for greater LSR counts for SOM nodes featuring stronger composite cyclones (lower and right rows; Fig. 4), we find that all nodes feature a mode in the lowest LSR count bin (less than 10 LSR events), and that the higher averages for the lower-right nodes arise from the right tail of the LSR distribution.

We also used a multivariate approach, training SOMs with normalized patterns of two or more variables. For example, an event-relative multivariate SOM trained on sea level pressure and 500-hPa geopotential height exhibits greater cyclone intensity in the lower right nodes (Fig. 5). Node-average LSRs counts for this SOM exhibit a broader range (12–71) relative to the SLP-only trained SOM (13–66; Figs. 2–4), but the LSR averages are not systematically structured across the SOM despite a general tendency for larger LSR averages where implied synoptic-scale forcing for ascent is stronger. The LSR distribution is focused in the immediate vicinity of the implied cold-frontal trough (Fig. 5), with less LSR density in the warm-frontal region despite strong warm advection suggested by geostrophic veering in many of the lower nodes.

It is also instructive to train SOMs with basic convective ingredients, such as CAPE (i.e., MUCAPE) and vertical wind shear, seeking tendencies for greater LSR frequency corresponding to larger CAPE and vertical wind shear. This exercise demonstrates that there is some tendency for greater LSR counts with higher CAPE (Fig. 6), but again the relation is not systematic, and maximum LSR density concentrates along the *gradient* of CAPE more than within regions of larger CAPE values. Of course, it is important to remember that we have eliminated high-CAPE cases from our database, which contributes to this distribution. The alignment of LSRs with CAPE gradients also suggests that severe convection is taking place in the presence of a lower-tropospheric frontal boundary, a location made more favorable for severe convection by the associated vertical wind shear and ascending motion associated with frontal circulations, which could also aid in the release of potential instability and locally enhance CAPE.

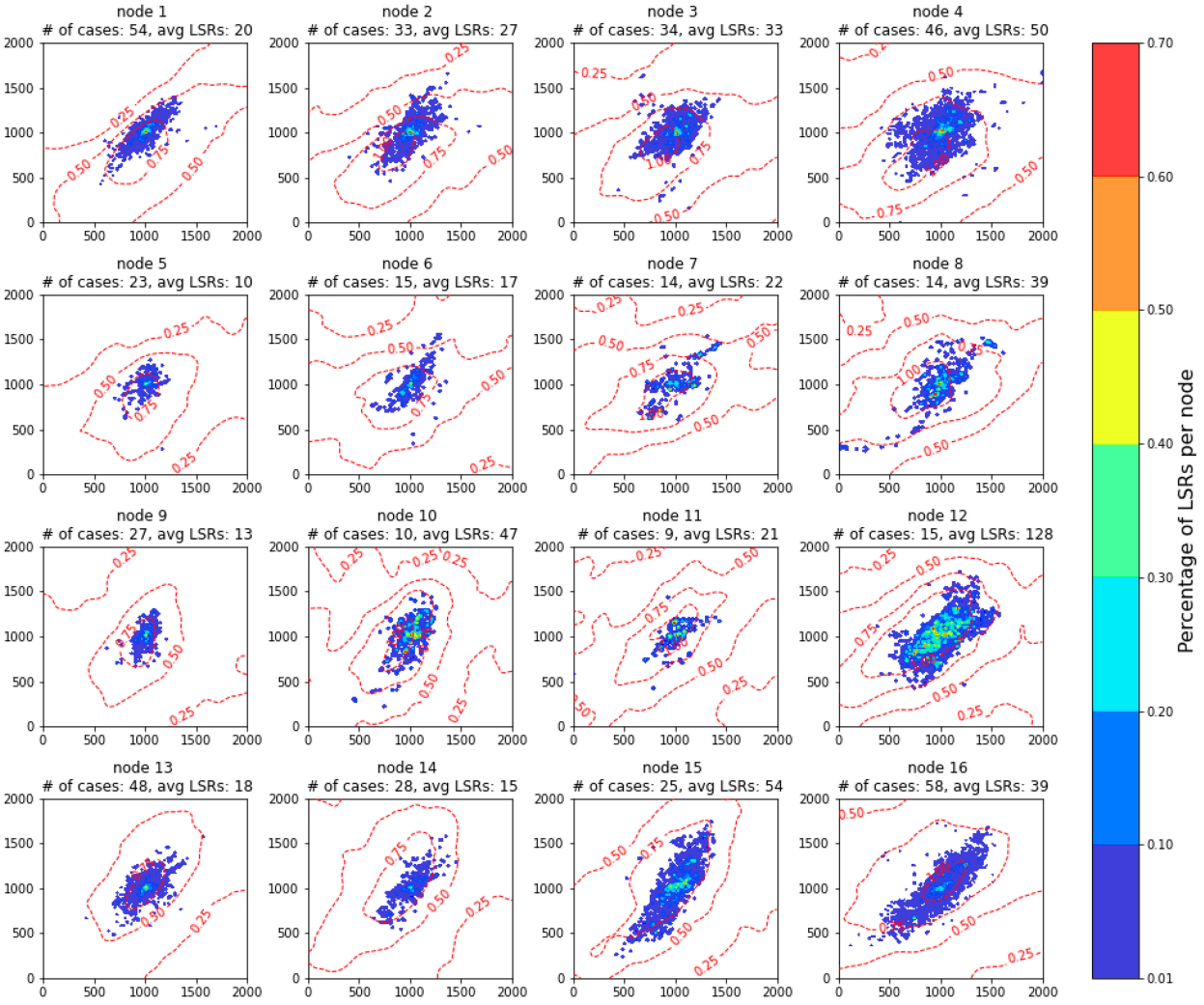

FIG. 10. SOM trained with SHERBS3; SHERBS3 is contoured in dashed red every 0.25. LSRs are plotted as in Fig. 2.

The relation between LSR occurrence and 0–6-km vertical wind shear also generally matches expectations, but again without a clear separation of high- and low-LSR frequency across nodes (Fig. 7). In some nodes, LSR density maximizes directly over the region of largest shear (lower right nodes), while in several other nodes, maximum LSR density is offset from the location of maximum shear (upper and left nodes). For the upper nodes, we speculate that the strongest shear is in the postfrontal region, with limited moisture and instability, and forcing for subsidence (not shown).

Using the 0–1-km shear (Fig. 8), a shear layer often maximized immediately ahead of cold fronts and identified as important in earlier studies (Sherburn et al. 2016), we see a greater spatial correspondence between large LSR density and the shear maxima. The magnitude of lower-tropospheric shear exhibits greater variability relative to the deep-layer shear, ranging from limited areas of shear > 20 kt (1 kt ≈ 0.51 m s^{-1}) to widespread regions of shear > 35 kt. The strong association between LSR density and lower-tropospheric shear underscores the importance of this quantity as a valuable predictor for HSLC severe convection, in keeping with prior studies (e.g., Sherburn and Parker 2014; Sherburn et al. 2016).

Several earlier studies have demonstrated the importance of the release of potential instability as a destabilization mechanism accompanying some HSLC severe events (Sherburn et al. 2016; King et al. 2017). To identify this process in proxy, we trained a multivariate SOM with 1000–700-hPa θ_e difference and gridscale 500-hPa vertical motion (Fig. 9). This SOM reveals considerable variations in pattern, with strong cold-frontal patterns implied in the lower left nodes (consistent with strong gradients in θ_e difference) and a suggestion of warm-frontal or frontal-wave type patterns in the lower-right nodes (implied by the east–west orientation of θ_e difference). Most nodes show at least some potential instability (θ_e decreasing with height from 1000 to 700 hPa) in the vicinity of the greatest LSR density, and the maximum LSR density also aligns with the largest 500-hPa upward vertical motion, consistent with a mechanism to release the instability.

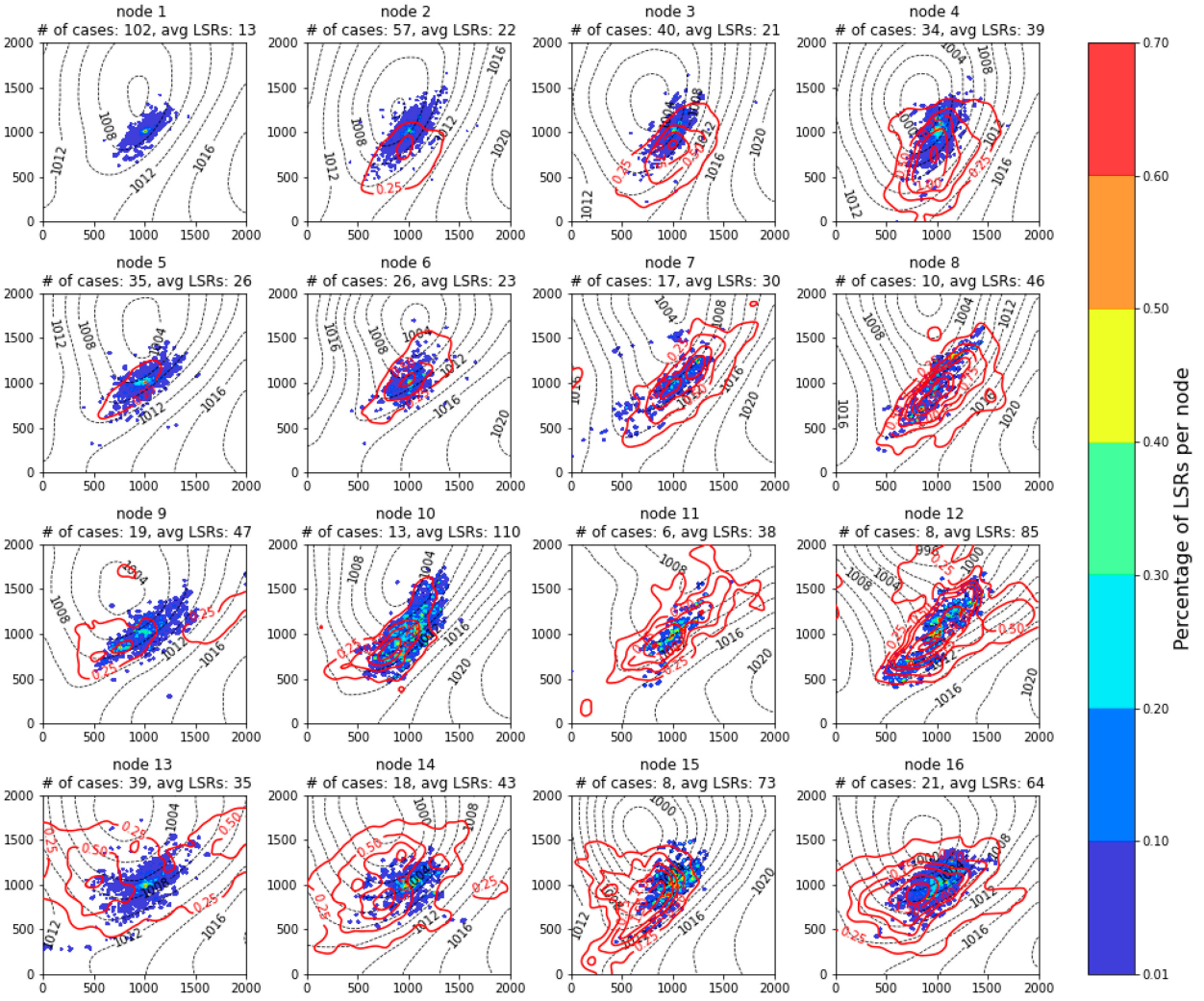

FIG. 11. SOM trained with MOSH from HSLC severe events. Data are event-relative 2000 km × 2000 km grids centered on the event-averaged storm report latitude and longitude. MOSH is contoured in red every 0.25, node composite SLP is contoured with dashed lines every 2 hPa, and LSRs are plotted as in Fig. 2. Node number, number of events per node, and the average number of wind and tornado LSRs for each node are listed above each node.

The SOMs presented thus far demonstrate strong event-relative alignment of synoptic-scale forcing for ascent and maximum LSR density. These results also demonstrate the complexity of HSLC environments, suggesting the benefits of using composite parameters described in prior studies, such as SHERBS3 and MOSH (Sherburn and Parker 2014; Sherburn et al. 2016). Training SOMs on these composite parameters and overlaying LSR density provides a useful check on their efficacy. A SHERBS3-trained SOM features LSR density maxima generally concentrated within local maxima of this parameter (Fig. 10). Training a SOM using MOSH also shows generally high spatial collocation of MOSH maxima and greatest LSR density (Fig. 11). Despite this, some nodes (e.g., 1, 9, 11, 12) show less MOSH–LSR overlap. Investigation of cases in these nodes indicates that some are due to boundary effects (no LSRs offshore). In summary, SOMs trained using SHERBS3 and MOSH both show promising correspondence between the distributions of these composite parameters and LSR density, reinforcing the value of these parameters for operational prediction. The SHERBS3, while exhibiting larger spatial coverage, is better aligned with LSR density maxima than MOSH in the cases considered in this study.

b. *Stratification by LSR count*

There are no true null events in the case catalog analyzed here, but we have set a very low case identification threshold, allowing large variations in severe occurrence within the catalog. Although the preceding analysis is generally consistent with the expected relationships between LSR density and basic HSLC convective ingredients, we have not yet identified distinct synoptic or mesoscale patterns accompanying high and low LSR activity within the set of HSLC severe events. To examine this possible environmental distinction using an alternate strategy, we stratified the HSLC events

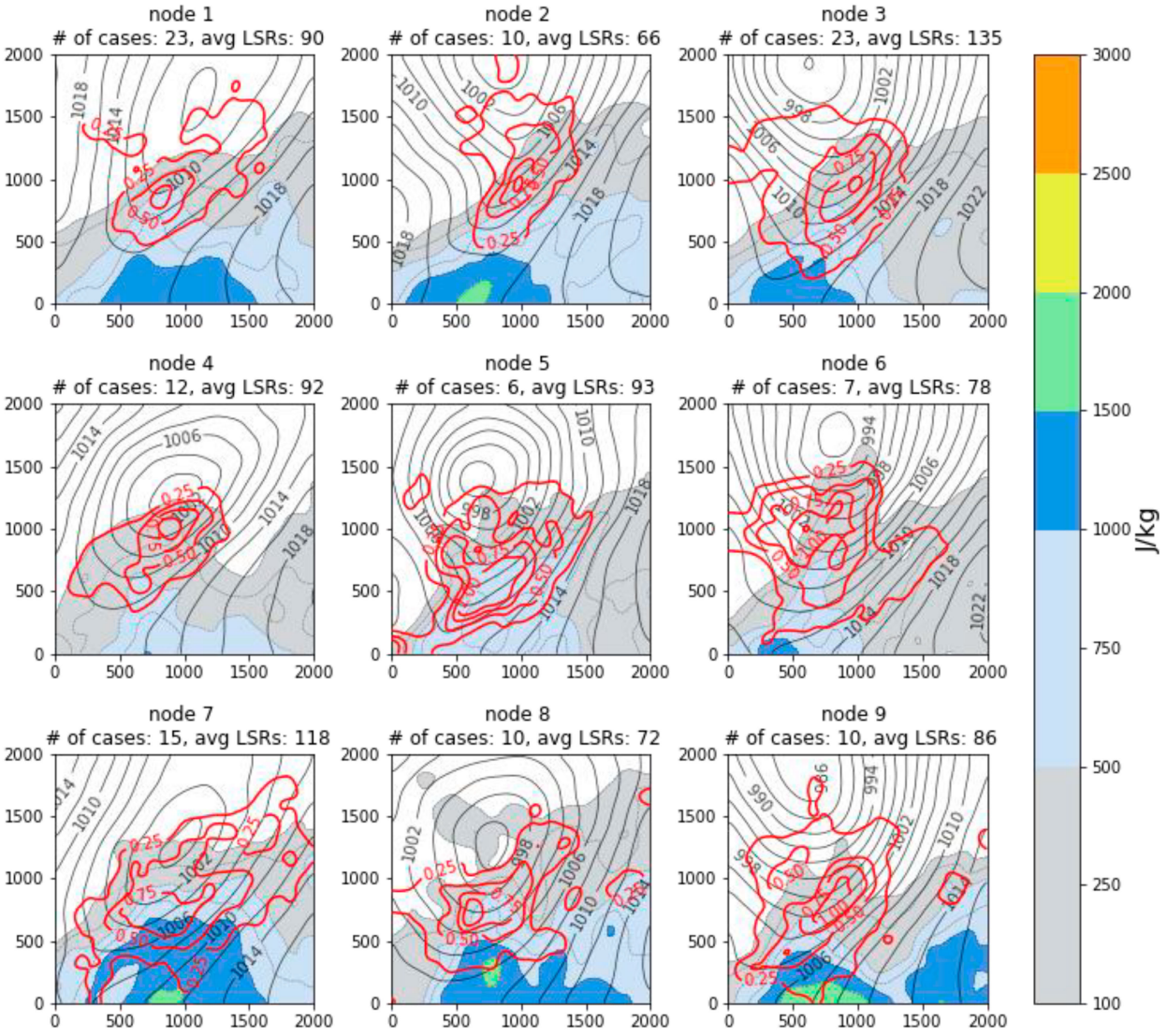

FIG. 12. SOM trained with sea level pressure (hPa) from HSLC severe events in the upper quartile of LSR occurrence. Data are event-relative 2000 km × 2000 km grids centered on the event-averaged storm report latitude and longitude. Pressure is contoured in black every 2 hPa, MUCAPE is shaded, as in the color bar, and MOSH is contoured in red every 0.25.

by LSR activity, training separate SOMs on events within the upper and lower quartiles of LSR frequency. We find that while the average cyclone intensity is stronger across nodes in the upper-quartile SLP SOM (Fig. 12) as opposed to its lower-quartile counterpart (Fig. 13), differences based on SLP alone are subtle; there are nodes featuring strong cyclones in both the lower- and upper-quartile SOMs (e.g., nodes in the lower left corner in Fig. 13).

The accompanying instability environments and composite MOSH provide a more illuminating representation of the differences between the upper- and lower-quartile events. On average, larger MUCAPE values extend father north (relative to the cyclone) in the upper-quartile SOM nodes (Fig. 12) than in the lower-quartile SOM (Fig. 13); quantitatively, the total area of MUCAPE > 500 J kg^{-1} is 63% greater in the upper-quartile SOM. There are also substantially greater MOSH values on average in the upper-quartile SOM, in which the MOSH maxima overlap with the tongue of northward extending instability (Fig. 12). Substantial MOSH values are not absent in the lower-quartile SOM (Fig. 13), but the composite average values in most nodes are well below the parameter threshold of 1.0 (this is in part due to variability and signal smoothing within each node).

Despite being separated by LSR occurrence, the SOM trained using upper-quartile 0–1-km vertical wind shear (Fig. 14) shows a strikingly similar distribution to that in the respective lower-quartile SOM (Fig. 15); quantitatively, the upper-quartile SOM features only a 39% greater area of shear > 20 kt. Both SOMs contain nodes with low-level wind shear exceeding 40 kt. However, in the lower-quartile SOM (Fig. 15), the strong shear nodes (1 and 4) are defined by a low-level jet east of the domain center with an associated

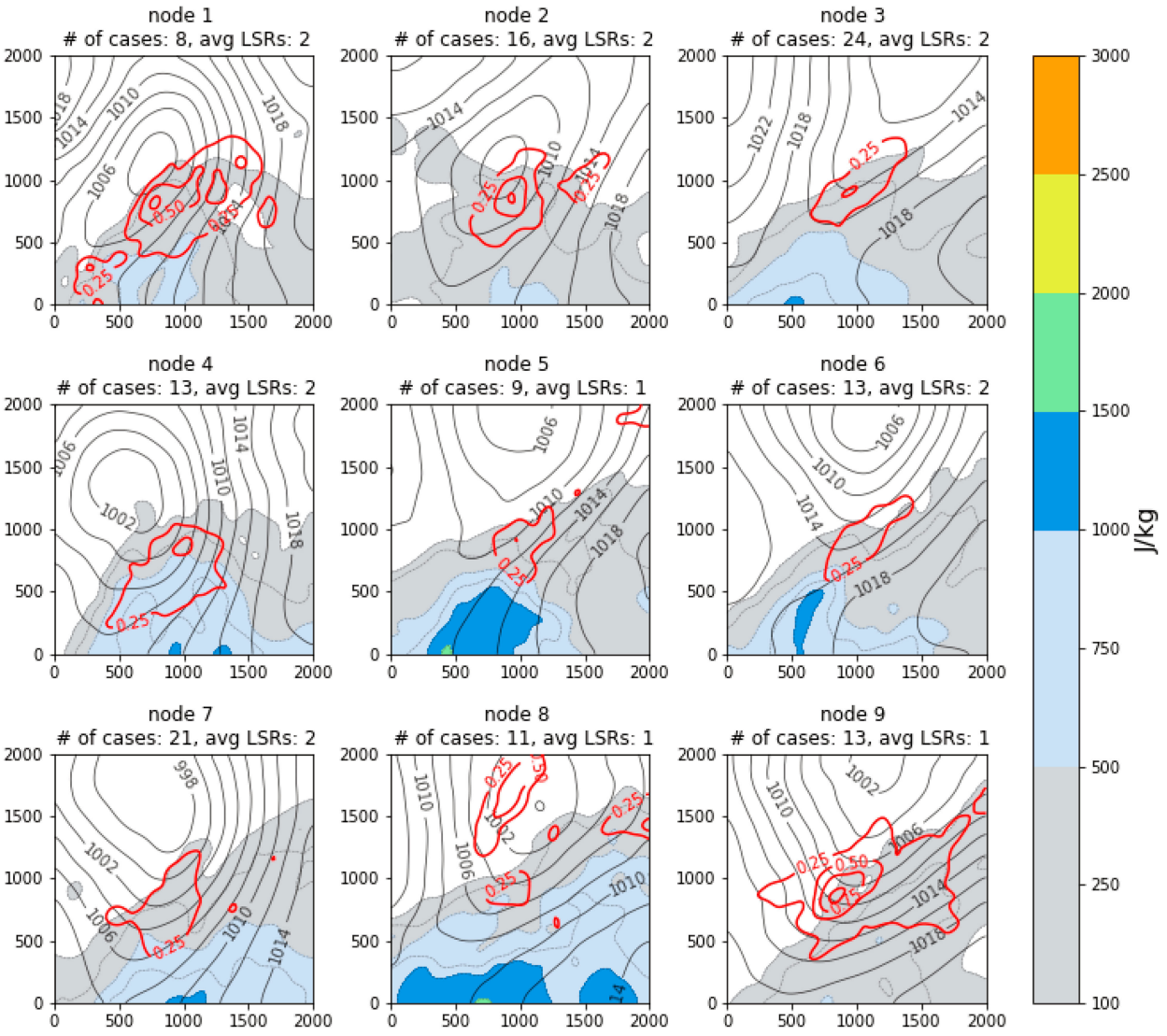

FIG. 13. As in Fig. 12, but for events in the lower quartile of LSR frequency.

more eastward located surface cyclone whereas in the upper-quartile SOM (Fig. 14), nodes with similar shear values (nodes 3, 6, 9) are represented by a centrally located low-level jet and surface cyclone. This result suggests that HSLC events with comparably fewer LSRs may be partly due to misaligned dynamical features. The upper-quartile SOM also contains a node of relatively low shear (node 7; 25 kt; Fig. 14) similar to the lower-quartile SOM (node 9; 20 kt). Because vertical wind shear is large for nearly all events, its distribution does not particularly distinguish high and low LSR frequency events.

Upper- and lower-quartile θ_e difference-trained SOMs show similar distributions in the strength and orientation of potential instability across all nodes (Figs. 16 and 17). However, more substantial differences between these SOMs are evident when the accompanying 500-hPa upward vertical velocity is considered. The upper-quartile SOM (Fig. 16) exhibits greater 500-hPa upward vertical velocity across most nodes relative to the corresponding lower-quartile SOM (Fig. 17). Potential instability is present in the lower-quartile SOM nodes, and is even ample in nodes 6 and 9, but the lack of accompanying upward vertical velocity to provide the release of potential instability is likely a contributing factor to reduced LSR frequency (Fig. 17). To quantify this, we compute the total area of potential instability release, defined by collocation θ_e decreasing with height and composite upward 500-hPa vertical velocity exceeding 3 μb s^{-1} (1 μb = 10^{-3} hPa). We find a 129% larger area of proxy potential instability release in the upper-quartile SOM relative to the lower. In summary, proxy variables representing potential instability release are substantially more evident in higher-impact events across the HSLC severe event dataset.

When comparing upper- and lower-quartile MOSH-trained SOMs, we find substantial spread in maximum MOSH values

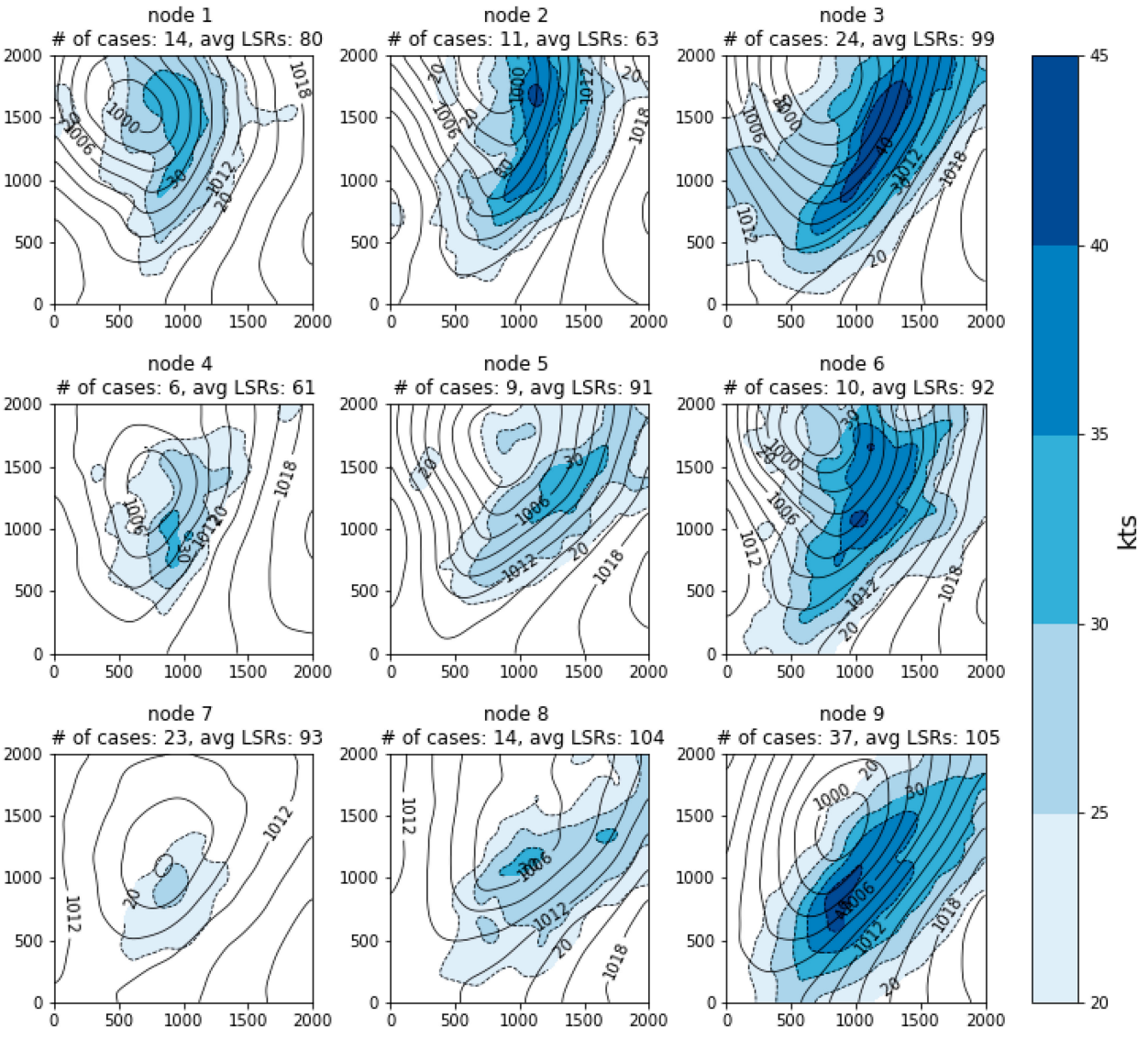

FIG. 14. SOM trained with 0–1-km vertical wind shear (kt) from HSLC severe events in the upper-quartile number of LSRs. Data are event-relative 2000 km × 2000 km grids centered on the event-averaged storm report latitude and longitude. Vertical wind shear is contoured and shaded, as in the color bar, and node-averaged sea level pressure is contoured in black every 2 hPa. The total number of events and the average number of wind and tornado LSRs for each node are listed above each node.

across nodes of the respective SOMs (Figs. 18 and 19). Spatial offsets between MOSH and LSR density maxima are evident in nodes 7 and 8 of the upper-quartile SOM (Fig. 18). However, on average across all nodes, the MOSH values associated with the upper-quartile MOSH SOM are considerably greater than in the lower-quartile SOM; we compute a 74% greater area of MOSH > 0.5 in the upper-quartile SOM. Given similar distributions of shear and lapse rates between the upper- and lower-quartile SOMs (not shown), the MOSH difference is associated with the greater amounts of potential instability and 500-hPa upward vertical velocity representing the release potential instability in the upper-quartile SOM. One reason for variability across nodes in each SOM is explained by the variability between individual events in a given node (not shown). Inspection of individual cases within node 9 in the upper-quartile MOSH SOM reveals cases featuring narrow regions of strong upward vertical velocity in potentially unstable environments, but the locations exhibit strong spatial variation. This results in equally narrow regions of high MOSH values that are smoothed out in the node composite, contributing to a greater area of MOSH > 0.5. Several nodes in the lower-quartile MOSH SOM have broad regions of high MOSH values, albeit of generally lower magnitude than the upper-quartile SOM, because they contain events with regions of significant upward vertical velocity in potential instability environments over a larger area. There is also some variability in 0–1-km vertical wind shear across nodes in this SOM (not shown), but the nodes with highest values of

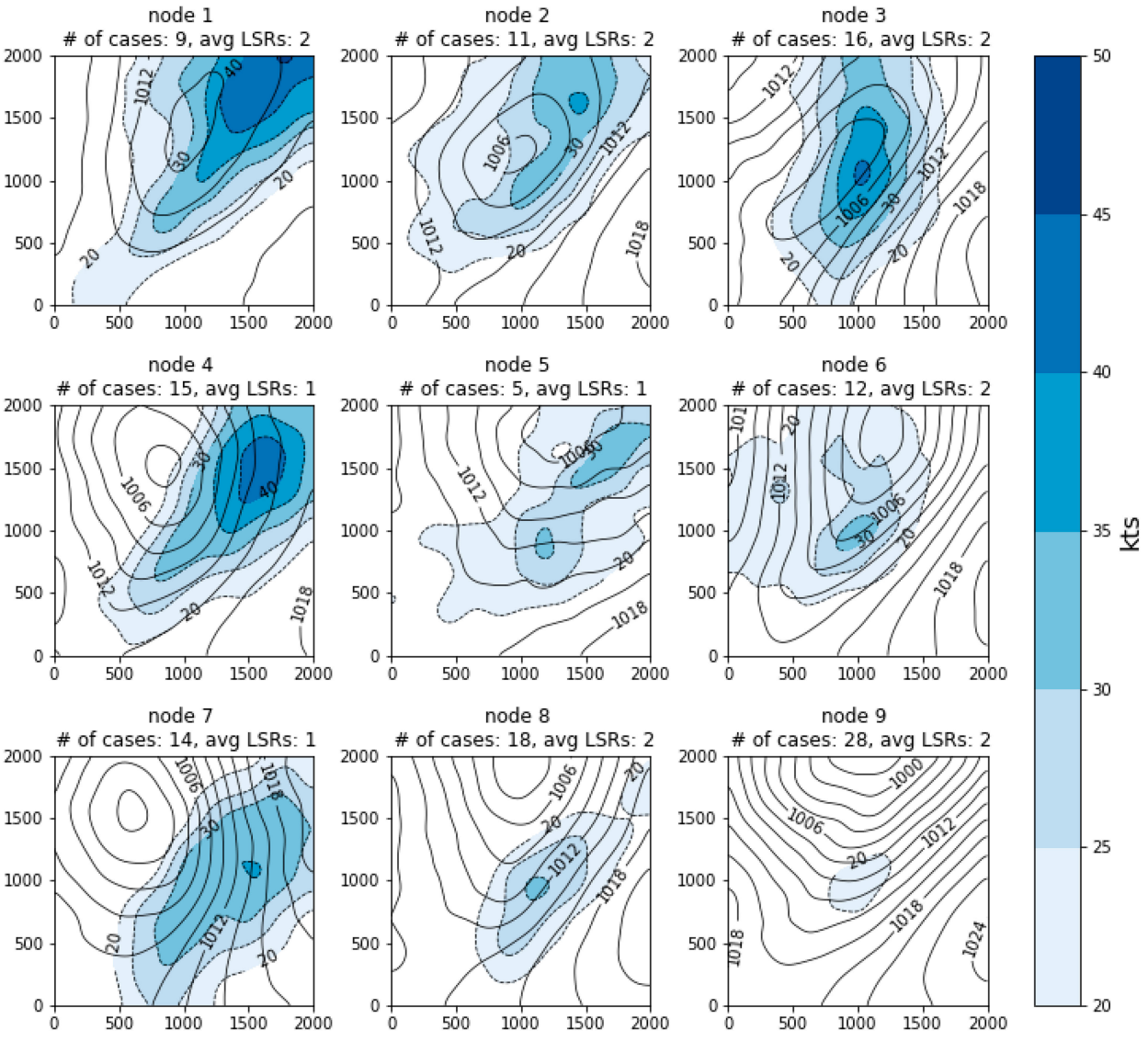

FIG. 15. As in Fig. 14, but for lower-quartile events.

0–1-km vertical wind shear are not consistently associated with nodes of high MOSH values. Over the entire HSLC severe event dataset, there are a few low-impact HSLC severe events that are defined by ample potential instability environments with sufficient vertical velocity forcing contributing to high values of MOSH. Aside from limitations associated with the LSR dataset, some of these events warrant individual examination in future case studies. On average, high values of MOSH are most associated with higher-impact HSLC severe events.

4. Conclusions

Severe convection in HSLC environments is a common threat to the southeastern United States and presents significant challenges to operational forecasters. Previous studies have assessed the patterns and ingredients of HSLC severe convection and examined the associated mechanisms in these environments (e.g., Sherburn and Parker 2014; Sherburn et al. 2016; King et al. 2017; Sherburn and Parker 2019). However, to the authors' knowledge, little work has been done to objectively classify the variations in synoptic-scale and mesoscale patterns that accompany HSLC severe convection. Here, we objectively classify these patterns, assess the distribution of severe weather occurrence across these patterns, and determine if these findings are consistent with previously developed HSLC composite parameters.

An automated, objective algorithm was developed to identify HSLC severe events using historical data from 2008 to 2021. Data sources included local storm reports along with RAP/RUC analyses (NCEI 2008; NOAA NCEP 2005). Owing to the extensive sample size, we used SOMs to identify characteristic patterns accompanying the HSLC events. We applied SOMs to classify the environmental patterns of 453

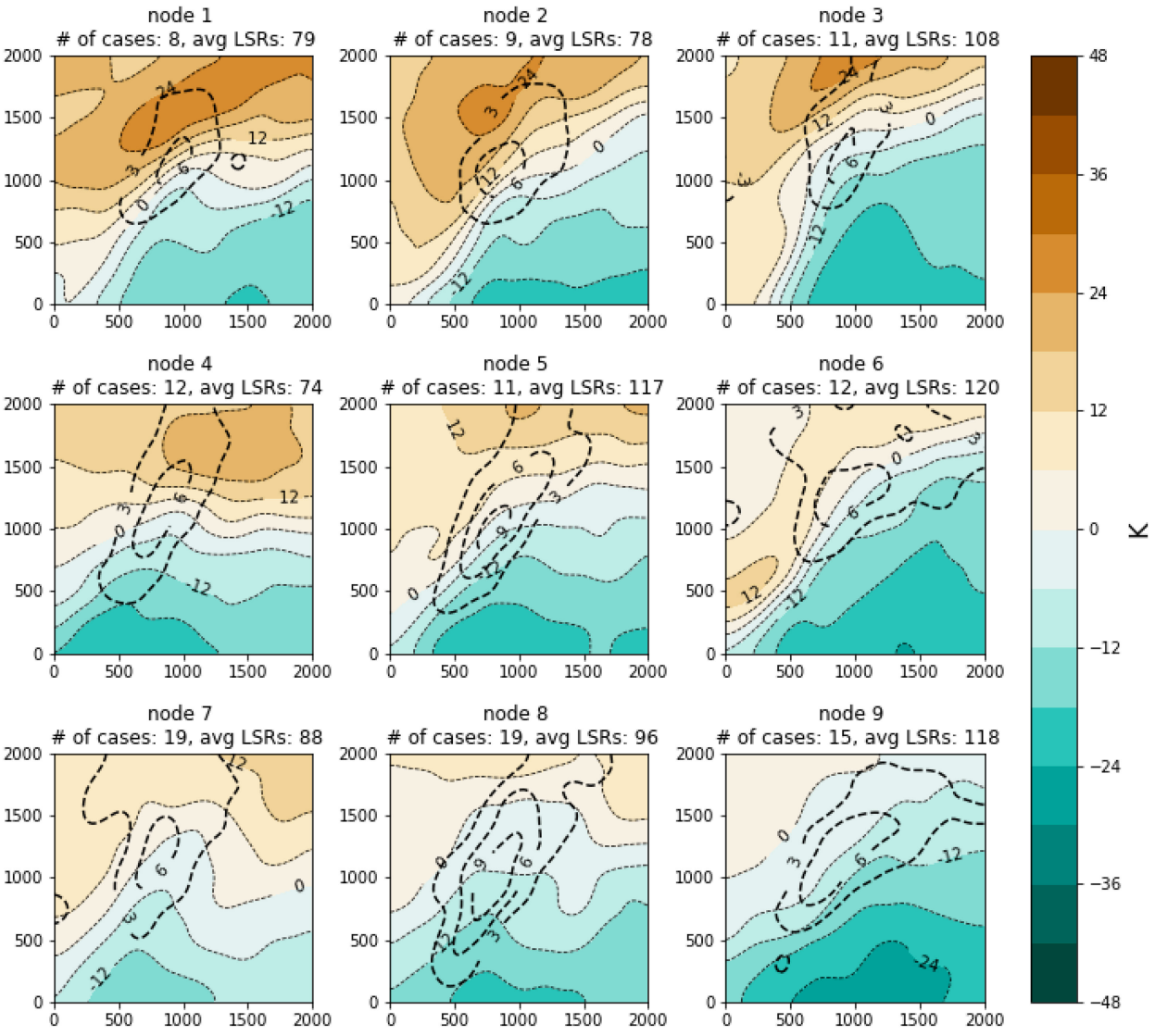

FIG. 16. SOM trained on 700–1000-hPa θ_e difference (K) from HSLC severe events in the upper-quartile number of LSRs. Data are event-relative 2000 km × 2000 km grids centered on the event-averaged storm report latitude and longitude. The θ_e difference is contoured and shaded, as in the color bar, and node-averaged upward 500-hPa vertical velocity is contoured in black every 3 μb s^{-1}. The total number of events and the average number of wind and tornado LSRs for each node are listed above each node.

HSLC severe events over 13 cool seasons. SOMs were trained on a set of 13 meteorological variables, selected based on the findings of previous HSLC literature (Sherburn and Parker 2014; Sherburn et al. 2016; King et al. 2017) to represent the variability in synoptic and mesoscale ingredients deemed influential to the production of HSLC severe convection. Our main findings are:

- Objectively classified meteorological patterns are consistent with previous HSLC environmental pattern studies, but SOMs provide insight into pattern variations:
  - The most common synoptic structure was a strong cyclone, with a north–south-oriented cold-frontal trough accompanied by a vigorous upper-tropospheric trough. Few events featured weaker cyclones west of the observation domain with an eastward extending trough (implied surface warm front). The region of maximum LSR density was predominantly located immediately east of an implied surface cold front (Figs. 2 and 5).
  - Events of all synoptic structures were generally characterized by a region of CAPE extending northward toward the center of LSR density maximum, with values varying from <500 J kg^{-1} to nearly 1000 J kg^{-1} (Fig. 2).
- The majority of HSLC severe events took place in the presence of potential instability superimposed with midtropospheric upward vertical velocity > 3 μb s^{-1}, consistent with the release of potential instability. Upward vertical velocity

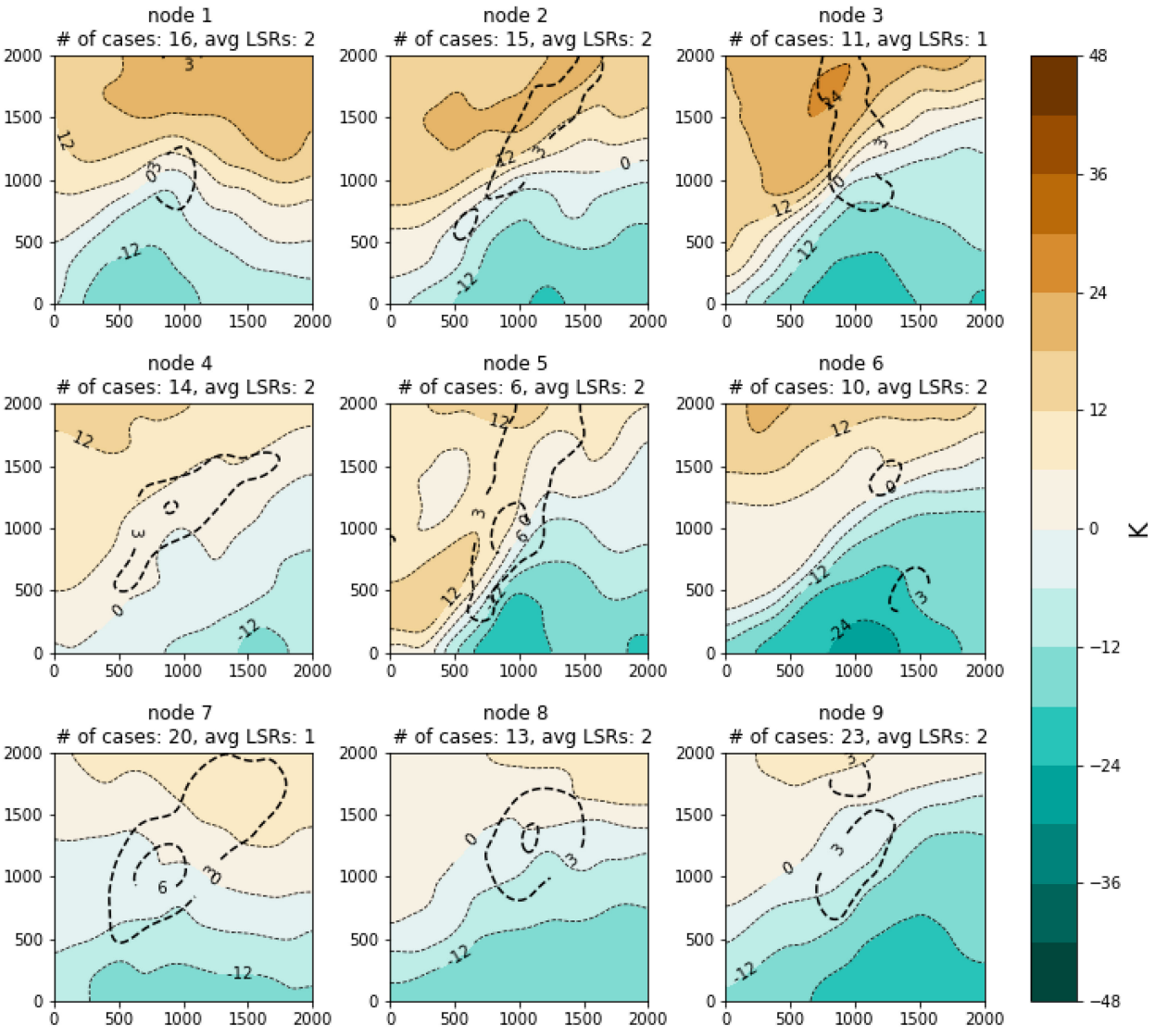

FIG. 17. As in Fig. 16, but for lower-quartile events.

was generally strongest in the presence of a strong potential instability gradient, aligned with an implied surface cold front (Fig. 9).

- Substantial deep-layer shear > 40 kt and lower-tropospheric wind shear > 20 kt were present in most cases, but the amount of lower-tropospheric shear exhibited greater variability, ranging from limited areas of shear > 20 kt to widespread regions of shear > 35 kt (Figs. 7 and 8).
- Maxima in SHERBS3 encompassed LSR maxima in a large majority of severe events. We found a high degree of variability in the representation of MOSH across events, with some MOSH nodes exhibiting a shift in MOSH maximum values from the LSR density center, or limited depiction of any substantial MOSH values altogether (Figs. 10 and 11).
- Stratifying by LSR activity suggests that the strength of potential instability release is a key discriminant between high- and low-activity HSLC severe events.

Accounting for potential instability release is a critical component in the MOSH composite parameter. As presented by Sherburn et al. (2016), MOSH is most skillful in distinguishing HSLC significant severe events from HSLC nonsevere events. While assessment of MOSH is subject to the limitations of this study, there are instances of lower-impact SOM nodes where MOSH values do not represent severe convection due to either averaging of spatially displaced cases or due to lower parameter values (Figs. 18 and 19). Despite this, MOSH was able to accurately depict HSLC severe convection in high-impact events on average, and showed strong contrasts between upper- and lower-quartile SOMs. In future work, it would be useful to analyze cases from the SOM nodes where the MOSH parameter did not match well with LSR density (aside from cases in which MOSH maxima fell outside of our LSR domain). MOSH and SHERBS3 are useful discriminators between significant severe and nonsevere HSLC events,

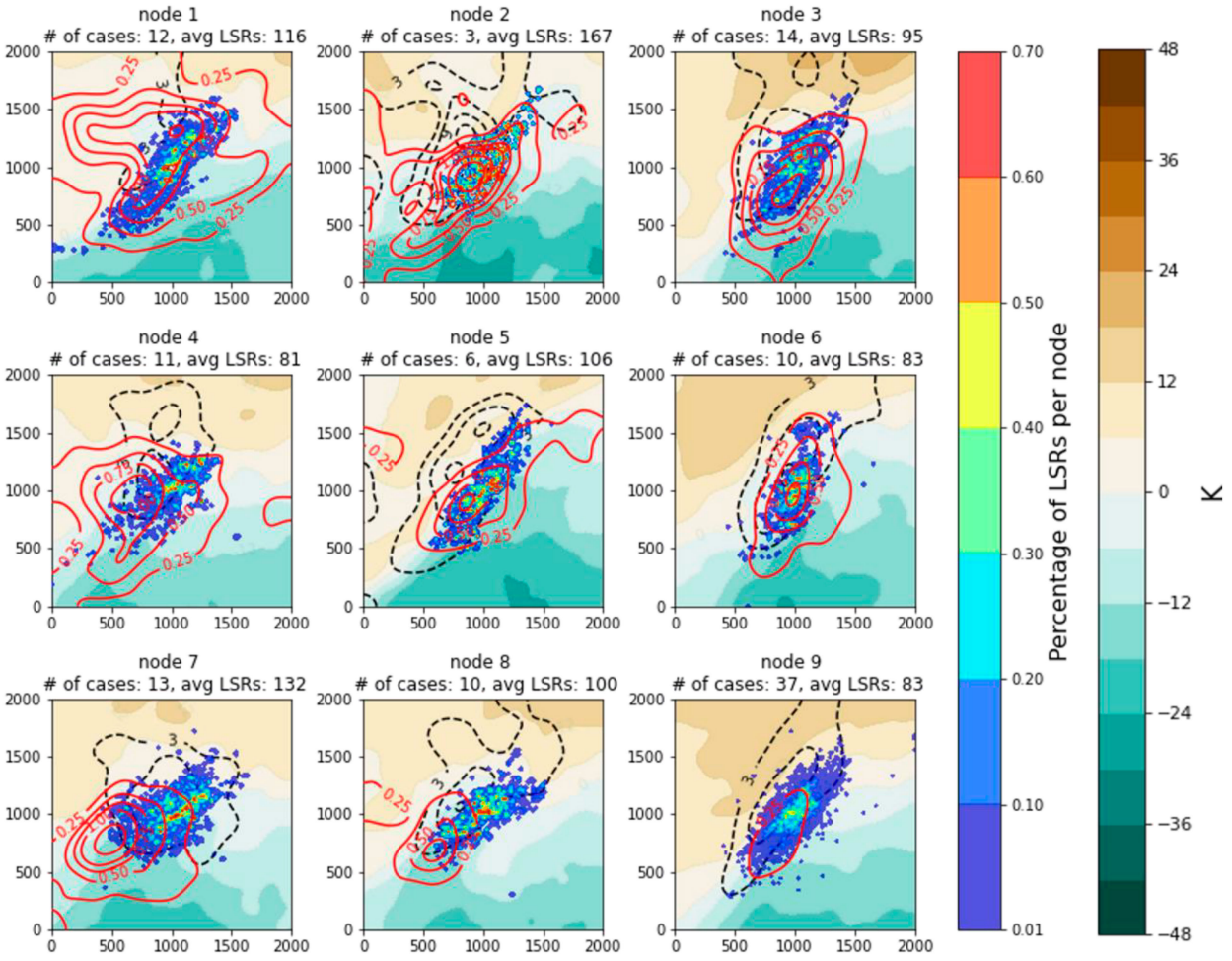

FIG. 18. SOM trained on MOSH from HSLC severe events in the upper-quartile number of LSRs. Data are event-relative 2000 km × 2000 km grid centered on the event-averaged storm report latitude and longitude. MOSH is contoured in red every 0.25, node composite θ_e difference is shaded every 6 K as in the legend, node composite upward 500-hPa vertical velocity is contoured in dashed black every 3 μb s^{-1}, and LSRs are plotted as in Fig. 2. The total number of events and the average number of wind and tornado LSRs for each node are listed above each node.

but discrepancies can occur because these composite parameters do not forecast whether convection will be initiated. Additionally, this study did not assess the SHERBE or MOSHE composite parameters, where effective bulk shear vector magnitude is incorporated into parameter calculation. The inclusion of these parameters may have provided additional distinction in environmental patterns or distributions of severe weather occurrence.

There are several important limitations of our study. Reliance on LSRs to identify severe convection has known issues, and an added difficulty in our study is the lack of LSRs over water. Stricter wind speed or tornado severity requirements could have been implemented to overcome the sources of error associated with LSRs (documented in section 2), or additional metrics such as radar reflectivity signatures or NWS warnings could have been used to supplement LSRs. In addition, the process of HSLC severe event identification was automated, and only the local CAPE and wind shear environments around LSRs were examined. Using these local environments for automated event identification could lead to discrepancies from a human's subjective impression of the regional environment. Future work could involve performing the same SOM analysis, but separating events into hourly increments (as LSRs allow) rather than characterizing the entire event by window onset time. NWS warning data could also allow for an improved aspect of predictability in future studies, including the definition of a null dataset (e.g., events featuring warnings but without LSRs). Using warning data in combination with LSRs and radar reflectivity signatures would also allow for computation of contingency metrics and quantitative assessment of forecasts. Another limitation relates to the somewhat coarse 20-km gridcell dimension of the RAP/RUC dataset. There are storm-scale features, such as cold-pool density gradients (e.g., McDonald and Weiss 2021) that could be important discriminators for QLCS severe weather but which are not resolved in these data. Perhaps

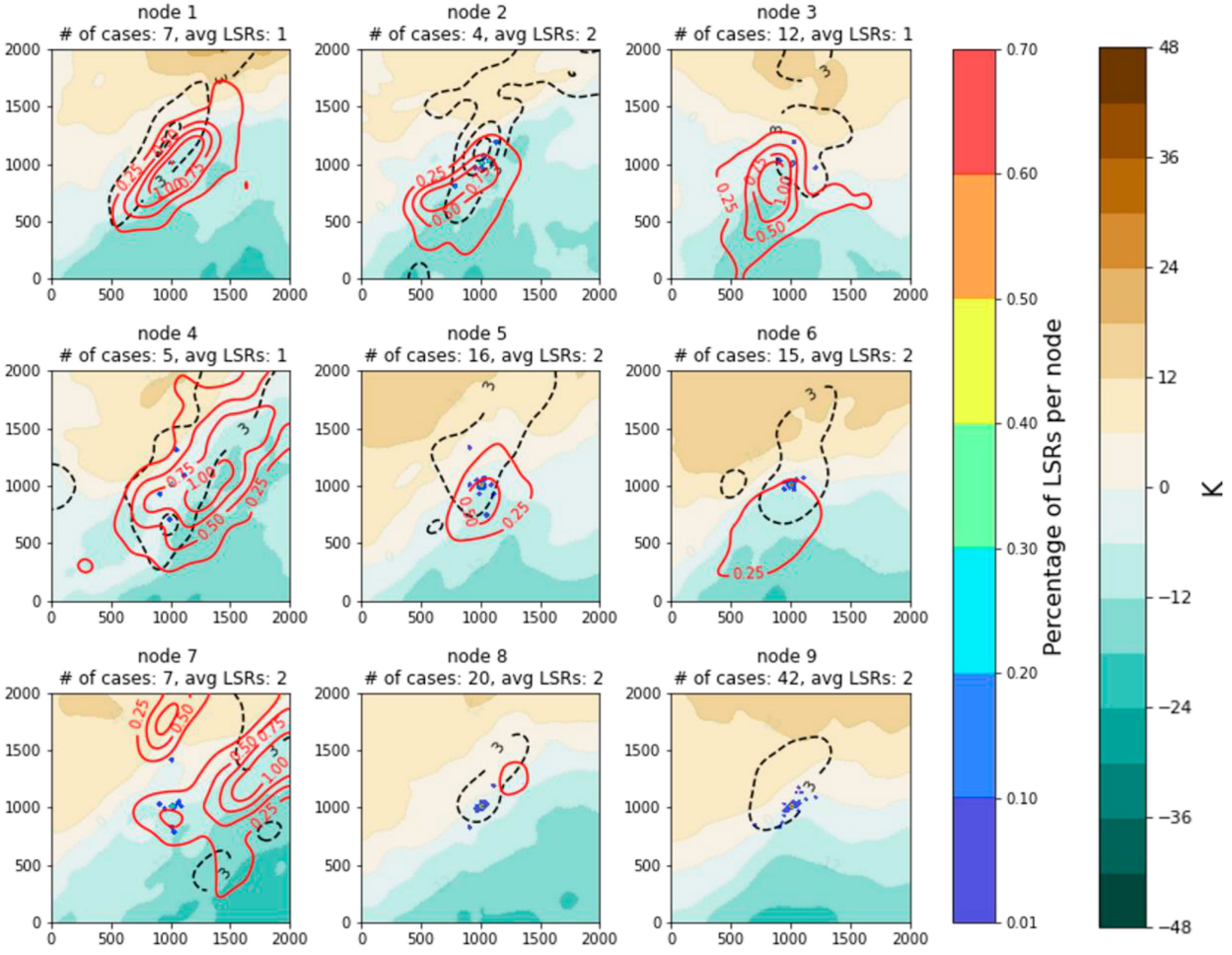

FIG. 19. As in Fig. 18, but for lower-quartile SOM.

repeating the analysis with High-Resolution Rapid Refresh (HRRR; Dowell et al. 2022; James et al. 2022) data would allow examination of this aspect.

Finally, there are limits to our study related to the capabilities of SOMs, particularly in relation to the need for extensive tuning of hyperparameters and human subjectivity in assessing whether SOM patterns are physically meaningful. Despite these limitations, use of SOMs to classify gridded fields in combination with storm reports has clarified the distribution of severe convective storms and the associated mechanisms for southeastern U.S. HSLC severe events. From our analysis, it is clear that severe convection in HSLC environments in this region occurs primarily in close association with cold fronts, and that the presence of potential instability release is a critical discriminant separating high- and low-impact cases.

Acknowledgments. This project was funded by NOAA CSTAR Grant NA17NWS4680002. In addition, G. M. L. was supported by NOAA CSTAR Grant NA19NWS4680001. M. D. P. received additional support for this effort from NSF Grant AGS-2020588. M. J. M. was supported by the U.S. Department of Energy, Office of Science DE-SC0022070 and NSF IA 1947282, and by the National Center for Atmospheric Research (NCAR), which is sponsored by the NSF. We acknowledge valuable input from Dr. Keith Sherburn (NWS) and Prof. Sandra Yuter (NCSU); special thanks to Keith Sherburn for providing material to help with the HSLC identification process and the implementation of MOSH and SHERBS3 in this study. We thank three anonymous reviewers for thoughtful and constructive comments and suggestions on an earlier draft of the manuscript.

Data availability statement. The source of local storm reports used in this study is https://www.spc.noaa.gov/wcm/, and gridded RUC and RAP data were obtained from https://www.ncei.noaa.gov/products/weather-climate-models/rapid-refresh-update

REFERENCES

Anderson-Frey, A. K., Y. P. Richardson, A. R. Dean, R. L. Thompson, and B. T. Smith, 2016: Investigation of near-storm

environments for tornado events and warnings. *Wea. Forecasting*, **31**, 1771–1790, https://doi.org/10.1175/WAF-D-16-0046.1.

——, ——, ——, ——, and ——, 2019a: Characteristics of tornado events and warnings in the Southeastern United States. *Wea. Forecasting*, **34**, 1017–1034, https://doi.org/10.1175/WAF-D-18-0211.1.

——, ——, ——, ——, and ——, 2019b: Self-organizing maps for tornadic near-storm environments of the Southeastern United States. *18th Conf. on Artificial and Computational Intelligence and Its Applications to the Environmental Sciences*, Phoenix, AZ, Amer. Meteor. Soc., 3A.5, https://ams.confex.com/ams/2019Annual/meetingapp.cgi/Paper/354039.

Ashley, W. S., 2007: Spatial and temporal analysis of tornado fatalities in the United States: 1880–2005. *Wea. Forecasting*, **22**, 1214–1228, https://doi.org/10.1175/2007WAF2007004.1.

——, A. J. Krmenec, and R. Schwantes, 2008: Vulnerability due to nocturnal tornadoes. *Wea. Forecasting*, **23**, 795–807, https://doi.org/10.1175/2008WAF2222132.1.

Brooks, H. E., C. A. Doswell III, and M. P. Kay, 2003: Climatological estimates of local daily tornado probability for the United States. *Wea. Forecasting*, **18**, 626–640, https://doi.org/10.1175/1520-0434(2003)018<0626:CEOLDT>2.0.CO;2.

Campbell, T. A., 2022: Self-organizing maps for classifying variability in Southeastern U.S. high-shear, low-CAPE environments. M.S. thesis, Dept. of Marine, Earth and Atmospheric Sciences, North Carolina State University, 131 pp., https://www.lib.ncsu.edu/resolver/1840.20/40067.

Clark, M. R., 2009: The southern England tornadoes of 30 December 2006: Case study of a tornadic storm in a low CAPE, high shear environment. *Atmos. Res.*, **93**, 50–65, https://doi.org/10.1016/j.atmosres.2008.10.008.

Davis, J. M., and M. D. Parker, 2014: Radar climatology of tornadic and nontornadic vortices in high-shear, low-CAPE environments in the mid-Atlantic and southeastern United States. *Wea. Forecasting*, **29**, 828–853, https://doi.org/10.1175/WAF-D-13-00127.1.

Dawson, L. C., G. S. Romine, R. J. Trapp, and M. E. Baldwin, 2017: Verifying supercellular rotation in a convection-permitting ensemble forecasting system with radar-derived rotation track data. *Wea. Forecasting*, **32**, 781–795, https://doi.org/10.1175/WAF-D-16-0121.1.

Dean, A. R., and R. S. Schneider, 2008: Forecast challenges at the NWS Storm Prediction Center relating to the frequency of favorable severe storm environments. *24th Conf. on Severe Local Storms*, Savannah, GA, Amer. Meteor. Soc., 9A.2, https://ams.confex.com/ams/24SLS/techprogram/paper_141743.htm.

——, and ——, 2012: An examination of tornado environments, events, and impacts from 2003–2012. *26th Conf. on Severe Local Storms*, Nashville TN, Amer. Meteor. Soc., P60, https://ams.confex.com/ams/26SLS/webprogram/Paper211580.html.

Doswell, C. A., 2001: Severe convective storms—An overview. *Severe Convective Storms, Meteor. Mongr.*, No. 50, Amer. Meteor. Soc., 1–26.

——, H. E. Brooks, and M. P. Kay, 2005: Climatological estimates of daily local nontornadic severe thunderstorm probability for the United States. *Wea. Forecasting*, **20**, 577–595, https://doi.org/10.1175/WAF866.1.

Dowell, D. C., and Coauthors, 2022: The High-Resolution Rapid Refresh (HRRR): An hourly updating convection-allowing forecast model. Part I: Motivation and system description. *Wea. Forecasting*, **37**, 1371–1395, https://doi.org/10.1175/WAF-D-21-0151.1.

Edwards, R., J. T. Allen, and G. W. Carbin, 2018: Reliability and climatological impacts of convective wind estimations. *J. Appl. Meteor. Climatol.*, **57**, 1825–1845, https://doi.org/10.1175/JAMC-D-17-0306.1.

Evans, M., 2010: An examination of low CAPE/high shear severe convective events in the Binghamton, New York County warning area. *Natl. Wea. Dig.*, **34**, 129–144.

Goldacker, N. A., and M. D. Parker, 2021: Low-level updraft intensification in response to environmental wind profiles. *J. Atmos. Sci.*, **78**, 2763–2781, https://doi.org/10.1175/JAS-D-20-0354.1.

Graham, C. S., 2021: Verification of convection-allowing NWP in southeastern U.S. high-shear, low-CAPE environments. M.S. thesis, Dept. of Marine, Earth and Atmospheric Sciences, North Carolina State University, 89 pp., https://www.lib.ncsu.edu/resolver/1840.20/39034.

Guyer, J. L., A. K. Kis, K. N. Venable, and D. A. Imy, 2006: Cool season significant (F2-F5) tornadoes in the Gulf Coast states. *23rd Conf. on Severe Local Storms*, St. Louis, MO, Amer. Meteor. Soc., 4.2, https://ams.confex.com/ams/23SLS/techprogram/paper_115320.htm.

Hewitson, B. D., and R. G. Crane, 2002: Self-organizing maps: Applications to synoptic climatology. *Climate Res.*, **22**, 13–26, https://doi.org/10.3354/cr022013.

James, E. P., and Coauthors, 2022: The High-Resolution Rapid Refresh (HRRR): An hourly updating convection-allowing forecast model. Part II: Forecast performance. *Wea. Forecasting*, **37**, 1397–1417, https://doi.org/10.1175/WAF-D-21-0130.1.

King, J. R., M. D. Parker, K. D. Sherburn, and G. M. Lackmann, 2017: Rapid evolution of cool season, low-CAPE severe thunderstorm environments. *Wea. Forecasting*, **32**, 763–779, https://doi.org/10.1175/WAF-D-16-0141.1.

Kis, A. K., and J. M. Straka, 2010: Nocturnal tornado climatology. *Wea. Forecasting*, **25**, 545–561, https://doi.org/10.1175/2009WAF2222294.1.

Kohonen, T., 2001: *Self-Organizing Maps*. 3rd ed. Springer, 501 pp.

LaFleur, A. T., R. L. Tanamachi, D. T. Dawson II, and D. D. Turner, 2023: Factors affecting the rapid recovery of CAPE on 31 March 2016 during VORTEX-Southeast. *Mon. Wea. Rev.*, **151**, 1459–1477, https://doi.org/10.1175/MWR-D-22-0051.1.

Lane, J. D., and P. D. Moore, 2006: Observations of a nonsupercell tornadic thunderstorm from terminal Doppler weather radar. *23rd Conf. on Severe Local Storms*, St. Louis, MO, Amer. Meteor. Soc., P4.5, https://ams.confex.com/ams/pdfpapers/115102.pdf.

Loikith, P. C., D. Singh, and G. P. Taylor, 2022: Projected changes in atmospheric ridges over the Pacific–North American region using CMIP6 models. *J. Climate*, **35**, 5151–5171, https://doi.org/10.1175/JCLI-D-21-0794.1.

Lovell, L. T., and M. D. Parker, 2022: Simulated QLCS vortices in a high-shear, low-CAPE environment. *Wea. Forecasting*, **37**, 989–1012, https://doi.org/10.1175/WAF-D-21-0133.1.

Markowski, P., and Y. Richardson, 2010: *Mesoscale Meteorology in Midlatitudes*. Wiley, 432 pp.

McCaul, E. W., and M. L. Weisman, 2001: The sensitivity of simulated supercell structure and intensity to variations in the shapes of environmental buoyancy and shear profiles. *Mon. Wea. Rev.*, **129**, 664–687, https://doi.org/10.1175/1520-0493(2001)129<0664:TSOSSS>2.0.CO;2.

McDonald, J. M., and C. C. Weiss, 2021: Cold pool characteristics of tornadic quasi-linear convective systems and other

convective modes observed during VORTEX-SE. *Mon. Wea. Rev.*, **149**, 821–840, https://doi.org/10.1175/MWR-D-20-0226.1.

Mechem, D. B., C. S. Wittman, M. A. Miller, S. E. Yuter, and S. P. de Szoeke, 2018: Joint synoptic and cloud variability over the Northeast Atlantic near the Azores. *J. Appl. Meteor. Climatol.*, **57**, 1273–1290, https://doi.org/10.1175/JAMC-D-17-0211.1.

NCEI, 2008: Storm events database. NOAA/NCEI, accessed 1 November 2023, https://www.ncdc.noaa.gov/stormevents/.

NOAA/NCEP, 2005: Rapid Refresh/Rapid Update Cycle. NOAA, accessed 17 March 2022, https://www.ncei.noaa.gov/products/weather-climate-models/rapid-refresh-update.

Nowotarski, C. J., and A. A. Jensen, 2013: Classifying proximity soundings with self-organizing maps toward improving supercell and tornado forecasting. *Wea. Forecasting*, **28**, 783–801, https://doi.org/10.1175/WAF-D-12-00125.1.

——, and E. A. Jones, 2018: Multivariate self-organizing map approach to classifying supercell tornado environments using near-storm, low-level wind and thermodynamic profiles. *Wea. Forecasting*, **33**, 661–670, https://doi.org/10.1175/WAF-D-17-0189.1.

Radford, J. T., and G. M. Lackmann, 2023: Assessing variations in the predictive skill of ensemble snowband forecasts with object-oriented verification and self-organizing maps. *Wea. Forecasting*, **38**, 1673–1693, https://doi.org/10.1175/WAF-D-23-0004.1.

Schneider, R. S., and A. R. Dean, 2008: A comprehensive 5-year severe storm environment climatology for the continental United States. *24th Conf. on Severe Local Storms*, Savannah, GA, Amer. Meteor. Soc., 16A.4, https://ams.confex.com/ams/24SLS/techprogram/paper_141748.htm.

——, ——, S. J. Weiss, and P. D. Bothwell, 2006: Analysis of estimated environments for 2004 and 2005 severe convective storm reports. *23rd Conf. on Severe Local Storms*, St. Louis, MO, Amer. Meteor. Soc., 3.5, https://ams.confex.com/ams/pdfpapers/115246.pdf.

Schuenemann, K. C., J. J. Cassano, and J. Finnis, 2009: Synoptic forcing of precipitation over Greenland: Climatology for 1961–99. *J. Hydrometeor.*, **10**, 60–78, https://doi.org/10.1175/2008JHM1014.1.

Sherburn, K. D., and M. D. Parker, 2014: Climatology and ingredients of significant severe convection in high-shear, low-CAPE environments. *Wea. Forecasting*, **29**, 854–877, https://doi.org/10.1175/WAF-D-13-00041.1.

——, and ——, 2019: The development of severe vortices within simulated high-shear, low-CAPE convection. *Mon. Wea. Rev.*, **147**, 2189–2216, https://doi.org/10.1175/MWR-D-18-0246.1.

——, ——, J. R. King, and G. M. Lackmann, 2016: Composite environments of severe and nonsevere high-shear, low-CAPE convective events. *Wea. Forecasting*, **31**, 1899–1927, https://doi.org/10.1175/WAF-D-16-0086.1.

Smith, B. T., R. L. Thompson, J. S. Grams, C. Broyles, and H. E. Brooks, 2012: Convective modes for significant severe thunderstorms in the contiguous United States. Part I: Storm classification and climatology. *Wea. Forecasting*, **27**, 1114–1135, https://doi.org/10.1175/WAF-D-11-00115.1.

Thompson, R. L., C. M. Mead, and R. Edwards, 2007: Effective storm-relative helicity and bulk shear in supercell thunderstorm environments. *Wea. Forecasting*, **22**, 102–115, https://doi.org/10.1175/WAF969.1.

——, B. T. Smith, J. S. Grams, A. R. Dean, and C. Broyles, 2012: Convective modes for significant severe thunderstorms in the contiguous United States. Part II: Supercell and QLCS tornado environments. *Wea. Forecasting*, **27**, 1136–1154, https://doi.org/10.1175/WAF-D-11-00116.1.

Trapp, R. J., D. M. Wheatley, N. T. Atkins, R. W. Przybylinski, and R. Wolf, 2006: Buyer beware: Some words of caution on the use of severe wind reports in post event assessment and research. *Wea. Forecasting*, **21**, 408–415, https://doi.org/10.1175/WAF925.1.

Vesanto, J., and E. Alhoniemi, 2000: Clustering of the self-organizing map. *IEEE Trans. Neural Networks*, **11**, 586–600, https://doi.org/10.1109/72.846731.

Vettigli, G., 2018: MiniSom: Minimalistic and NumPy-based implementation of the Self Organizing Map. Accessed 30 June 2021, https://github.com/JustGlowing/minisom.

Wade, A. R., and M. D. Parker, 2021: Dynamics of simulated high-shear low-CAPE supercells. *J. Atmos. Sci.*, **78**, 1389–1410, https://doi.org/10.1175/JAS-D-20-0117.1.

Weisman, M. L., and R. J. Trapp, 2003: Low-level mesovortices within squall lines and bow echoes. Part I: Overview and dependence on environmental shear. *Mon. Wea. Rev.*, **131**, 2779–2803, https://doi.org/10.1175/1520-0493(2003)131<2779:LMWSLA>2.0.CO;2.